

POLITECNICO DI TORINO

Master's Degree
in Mechatronic Engineering



**Politecnico
di Torino**

Master's Degree Thesis

Experimental test bench for electrodynamic levitation system characterization

Supervisor:
Prof. Andrea Tonoli
Prof. Nicola Amati
Dr. Angelo Bonfitto
Dr. Renato Galluzzi
Dr. Salvatore Circosta

Candidate:
Arianna Conchin Governati

A.Y. 2021/2022

Abstract

In recent years, globalisation and the focus on climate issues have led several governments to invest in faster, safer, and less polluting transport systems. Hyperloop Transportation Technology stands at the centre of this scenario due to its ability to reach very high speeds by exploiting electrodynamic phenomena between the track and the magnets attached to the train capsule. One of the most important factors on which the feasibility of the project depends, and on which most contemporary studies are focusing, is the stability of the system. State of art literature has shown that the unstable nature of magnetic levitation systems depends on the strong interaction between the electrodynamic and mechanical domains. This instability can be identified using a lumped-parameter model with multiple branches and can be removed by adding damping through a secondary suspension.

Another important aspect is to analyse how the lift and drag forces to which the magnetic levitation system is subjected vary according to the speed and distance between the track and the magnets.

After a brief literature review, to validate electrodynamic levitation, a dedicated test bench is proposed: some of its elements, such as load cells, aluminum track and copper rim, are characterized and the procedure followed to create a 90° Halbach array is illustrated. Afterwards, the thesis is divided into two main parts: the first one concentrates on the quasi-static experiment and the lift and drag curves to which the 90° Halbach array is subject are analysed for different gaps and angular velocities of the test bench. In the second part, starting from the experimental data, using a multidomain approach and performing the root locus, an optimal value of damping necessary to stabilise the system is found. Subsequently, the use of a voice coil as a damper is justified and an attempt is made to characterise its most important quantities such as resistance, inductance, and intrinsic damping, which do not remain linear during its operation time. Finally, two possible control solutions that could be implemented on a dedicated control unit and on the test bench are illustrated.

Acknowledgements

Questa tesi la dedico a tutte le persone che mi hanno accompagnata in questi anni di università.

In particolare la dedico alla mia famiglia.

A mio papà: sono orgogliosa di te e di come hai curato i tuoi pazienti durante il periodo di covid.

A mia mamma che mi ha coccolata in questi anni in cui sono tornata a casa e che non smette di farlo ancora ora.

A mia sorella che, nonostante il piccolo Alessandro, continua a trovare il tempo per aiutarmi ed ascoltarmi.

A Matteo e al nostro primo anno di convivenza.

A tutti i miei amici, soprattutto Erika, che nonostante la distanza è sempre presente.

Infine ringrazio tutti i professori e i ragazzi del LIM del Politecnico di Torino che hanno accompagnato me e Andrea nel nostro percorso di tesi: in particolare il dr Galluzzi ed Eugenio che sono stati sempre pronti ad aiutarci.

Contents

List of Tables	v
List of Figures	viii
Acronyms	ix
1 Introduction	1
1.1 Magnetic levitation transport systems	1
1.2 Hyperloop transportation system	1
1.2.1 Levitation system	2
1.3 Scientific research review	2
1.3.1 Multidomain approach	3
1.4 Thesis goal	5
1.4.1 Outline	5
2 Test bench characterization	7
2.1 Main frame	7
2.2 Quasi-static measurement system	7
2.3 Load cell characterization	9
2.3.1 Load cell framework	9
2.3.2 Load cells interference modelling	10
3 Aluminum disk and copper rim characterization	20
3.1 Aluminum rotor height measurement	20
3.2 Copper rim height measurement	21
4 Halbach array	25
4.1 Halbach array single assembly procedure	26
4.2 Halbach arrays assembly procedure	30
4.3 Halbach array assembly procedure on a pad	31
4.4 Non idealities sources	33

5	Quasi-static experiment	36
5.1	Instrumentation set-up	37
5.2	Experimental results	39
5.2.1	Time behaviour	39
5.2.2	Speed behaviour	41
5.2.3	Uncertainty zone	41
5.2.4	Lift to drag ratio	42
5.2.5	Scaled results	42
5.2.6	COMSOL simulation and experimental results comparison	43
5.2.7	Temperatures	44
6	Dynamic analysis	48
6.1	Dynamic measurement system	48
6.2	Fitting analysis	50
6.3	Root locus	52
6.4	Voice coil	53
6.4.1	General overview	53
6.4.2	Voice coil characterization	55
6.5	Control strategies	57
6.5.1	RL estimator circuit	57
6.5.2	Kalman Filter estimator	61
6.5.3	Comparison between RL and KF estimator	66
7	Conclusions and further studies	68
A	2 DOF state-space representation for stability analysis	70
	Bibliography	72

List of Tables

1.1	Levitation forces parameters	5
2.1	Sample masses parameters	10
2.2	Measurement point forces	13
2.3	Lift configuration angular coefficients and offsets	14
2.4	Drag configuration angular coefficients and offsets	15
5.1	Copper track and pad temperature during quasi-static experiment	47
6.1	Fit error, resistance and inductance with the different number of branches	52
6.2	Voice coil Geeplus TM parameters	54
6.3	Voice coil fitting parameters	57

List of Figures

1.1	<i>Hyperloop</i> passenger transport capsule conceptual design . . .	2
1.2	Lumped-parameter model	4
2.1	Test bench main frame drawing	7
2.2	Real test bench layout	8
2.3	Quasi-static measurement system	9
2.4	Real quasi-static measurement system	9
2.5	Load cell	10
2.6	Load cell framework	11
2.7	Samples masses	11
2.8	Load cells characterization	12
2.9	Load cells errors	12
2.10	Lift configuration setup	13
2.11	Lift configuration measurements	14
2.12	Lift configuration measurement fitting	15
2.13	Cell 1 offsets vs the applied forces in the lift direction	16
2.14	Drag configuration setup	17
2.15	Drag configuration measurements	17
2.16	Drag configuration measurement fitting	18
2.17	Cell 2 offsets vs the applied forces on drag direction	18
2.18	Drag configuration results and magnitude errors on cell 1 before and after the correction	19
2.19	Drag configuration results and magnitude errors on cell 2 before and after the correction	19
3.1	Vogel digital dial indicator	20
3.2	Aluminum rotor height measurements setup	21
3.3	Aluminum rotor measurement results	22
3.4	Copper rim height measurements setup	22
3.5	Copper rim measurement points	23
3.6	a) Qualitative trend of the copper rim: 3D analysis	23
3.7	b) Qualitative trend of the copper rim: 2D analysis	23
3.8	Copper rim defect	24

4.1	Halbach array configurations	25
4.2	Magnets properties	26
4.3	Materials for a single Halbach array	27
4.4	Single Halbach array assembly procedure: step 1	28
4.5	Single Halbach array assembly procedure: step 2	28
4.6	Single Halbach array assembly	29
4.7	Single Halbach array	30
4.8	Halbach array assembly procedure: step 2	31
4.9	Halbach array assembly procedure: step 3	32
4.10	Halbach array assembly	32
4.11	Halbach array	33
4.12	Halbach array assembly on a pad: step 1	33
4.13	Halbach array assembly on a pad: step 2	34
4.14	Final pad	34
4.15	Magnetic flux density comparison	35
4.16	Yaw, roll and pitch angle	35
5.1	Quasi-static acquisition procedure	36
5.2	Quasi-static acquisition setup	37
5.3	Electric motor management	38
5.4	Kollmorgen WorkBench setup	39
5.5	SCADAS setup	40
5.6	Quasi-static time response	41
5.7	Lift and drag forces time response	42
5.8	Lift and drag forces speeds response	43
5.9	Uncertainty zone	44
5.10	Lift to drag ratio	45
5.11	Scaled lift and drag curves	45
5.12	Scaled lift and drag curves behaviour	46
5.13	Example of Fluke temperature image	47
6.1	Dynamic measurement system	49
6.2	Experimental data vs lumped-parameter model	51
6.3	Fit error vs number of branches	52
6.4	Root locus without damping	53
6.5	Root locus as a function of the suspension damping	54
6.6	Root locus with optimal damping	55
6.7	Optimal suspension damping and damping ratio	56
6.8	Voice coil schematic representation	57
6.9	Voice coil Geeplus TM	57
6.10	Voice coil intrinsic damping characterization	58
6.11	Voice coil fully retracted position	59
6.12	0 - 4.52 Voltage step curves example	59
6.13	SIMULINK [®] Voice coil circuit	60

6.14	SIMULINK [®] RL circuit estimator	60
6.15	Multibody [™] voice coil	61
6.16	Multibody [™] velocity and RL estimated velocity without noise	62
6.17	Magnitude and phase Bode of RL estimator without noise	62
6.18	Multibody [™] velocity and RL estimated velocity with noise	63
6.19	Magnitude and phase Bode of RL estimated velocity with noise	63
6.20	SIMULINK [®] Kalman Filter	64
6.21	Multibody [™] velocity and KF estimated velocity without noise	65
6.22	Magnitude and phase Bode of KF estimator without noise	65
6.23	Multibody [™] velocity and KF estimated velocity with noise	66
6.24	Magnitude and phase Bode of KF estimator with noise	67

Acronyms

EDB: electro-dynamic bearings

DOF: degree of freedom

PM: permanents magnets

EMF: electromagnetic force

KF: Kalman Filter

Chapter 1

Introduction

1.1 Magnetic levitation transport systems

In recent decades, globalisation and the growing climate crisis have prompted several governments to invest in renewable resources: an example is the Strategic Transport Research and Innovation Agenda (STRIA) of the European Union that deals with smart and sustainable mobility [1, 2]. The transport systems are in the center of this revolution to achieve more efficient and lower emission technologies. For these reasons, nowadays, the efforts of engineers and scientists are directed towards developing magnetic levitation based systems, the so called *maglev* trains: using electromagnetic phenomena to levitate above the tracks on which they travel, they can reach speeds up to 600 km/h with a fully electrical propulsion. This kind of transportation systems brings several advantages, such as, low air pollution, reduction of maintenance costs due to the absence of rolling friction that makes the train very quiet and provides a very smooth ride for passengers. On the other hand, the greatest obstacle to the development of *maglev* systems is that they require entirely new infrastructure that cannot be integrated with existing ones. In this scenario, the *Hyperloop* concept ran as one of these possible future transportation systems.

1.2 Hyperloop transportation system

Based on Robert Goddard's *vactrains*, i.e. *vacuum tube trains* [3], the *Hyperloop* idea was introduced at the *All Things Digital Conference* and proposed in a white paper published by *SpaceX* in 2013 [4]: the *maglev* idea was improved introducing the use of low-pressure tubes in which the levitating capsules, propelled by an electric motor, travel subjected to minimal air drag force, allowing the trains to achieve speeds in excess of 1200 km/h (figure 1.1 shows the *Hyperloop* passenger transport capsule conceptual design).

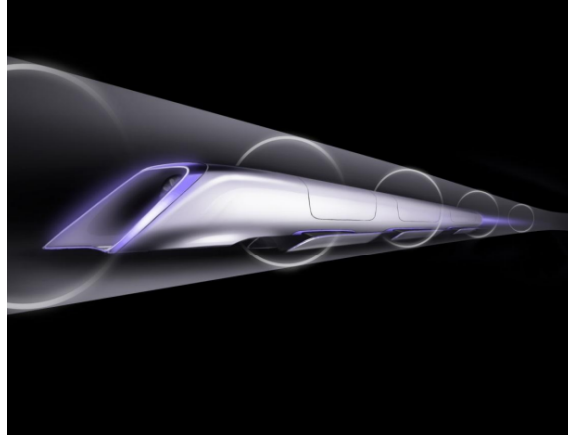


Figure 1.1: *Hyperloop* passenger transport capsule conceptual design

1.2.1 Levitation system

The use of wheels is made impossible due to the high speeds, so, in the first project, the capsule levitated through air bearings; then, the idea evolved by replacing the air bearings with magnetic pads; their use is based on the *Inductrack concept* [5] and on the electrodynamic levitation: the relative movement between the capsules with permanent magnets and the conducting tracks induces eddy currents as result of the Faraday-Lenz law; as a consequence, the capsule is affected by two forces:

- *lift* force F_L , on the vertical direction, responsible for the levitation;
- *drag* force F_D , a friction force since it acts in the opposite direction to the motion of the train.

PM based levitation system involves great advantages, such as, large air gaps, self-reliability and simplicity. Moreover, it is a fully passive system, so no cooling systems are needed [6]; another important aspect for very high-speed transportation technology is that the lift-to-drag ratio increases with speed. Unfortunately, as drawback, these systems are intrinsically unstable.

1.3 Scientific research review

Since the technology required to implement the *Hyperloop* project would revolutionise many areas, past scientific research have dealt with the infrastructure [7], aerodynamics of the system [8] and propulsion [9, 10]. Instead, the most recent ones have focused on the electrodynamic levitation [11] and, in particular, on finding a solution to its instability behaviour.

Tonoli et al. [12, 13, 14, 15], Filatov and Maslen [16], and Lembke [17, 18, 19, 20] research efforts were on modelling different configuration of the EDB's

to study stabilisation techniques.

Van Verdegheem et al., instead, have investigated rotating systems with EDB's [21] determining numerically the minimum amount of damping required for stabilization.

Regarding the translational variant of the EDB's, Post and Ryutov [22] have modelled its unstable behaviour without observed it with experiments.

Recently, Guo et al. studied the static force characteristics using an equivalent circuit to model the levitation phenomenon or a vector potential approach to optimise the geometry and the levitation of the system [23, 24, 25].

Wang et al. proposed a two DOF model that accurately reproduces the electrodynamic levitation behaviour (oscillations are present in the transient-time response) but it is not suitable for demonstrate the unstable behaviour of the levitation systems [26, 27].

In both the above research, the instability problem was not discuss.

Neither of these studies take into account the mechanical dynamic behaviour of the system where, instead, the instability takes place: in fact, the unstable nature in the magnetic levitation systems arises from the strong interaction between the electrodynamic and the mechanical domain.

1.3.1 Multidomain approach

A multidomain approach able to describe the electrodynamic levitation phenomenon when coupled with the mechanical domain was proposed by Galuzzi et al. and Circosta et al. [28, 29]: in these studies, the nonlinear electrodynamic levitation phenomenon is discretised using a lumped-parameter model, so that, the dynamic behaviour of the current inside the track conductor is represented as a multiple branch RL circuit. Comparing the results from the FE model and the lumped-parameter model, a suitable number of branches N_b that optimises the fitting quality can be found.

Let's consider an Halbach array of NdFeB permanent magnets (PM) (whose in-depth description will be covered in chapter 4) as proposed by Post [30], and a track made by aluminum that follows the specifications provided by *SpaceX* for the *Hyperloop* Pod Competition [31]: both the PM array and the aluminum slab are subjected to electromagnetic phenomena based on: the relation between the magnetic field \mathbf{H} and the current density \mathbf{J} in each medium (equation 1.1), the Lorentz force (equation 1.2) used to compute the current density distribution inside the track due to the velocity vector \mathbf{v} of the aluminum track and the Ampere's law (equation 1.3):

$$\nabla \times \mathbf{H} = \mathbf{J} \quad (1.1)$$

$$\mathbf{J} = \sigma(\mathbf{v} \times \mathbf{B}) \quad (1.2)$$

$$\mathbf{B} = \mu_0 \mu_r \mathbf{H} \quad (1.3)$$

The equations 1.1, 1.2 and 1.3 represent the intrinsic nonlinear nature of the electrodynamic phenomenon due to the strong interaction between the mechanical and the electrical domain. In order to analyse the dynamic behaviour of the system, Galluzzi et al. [28] propose to linearize the system using the lumped parameter method: the model consists of a number of parallel branches N_b , each with its own resistivity R_k and inductance L_k (figure 1.2).

In this way, the continuous current density distribution is discretized.

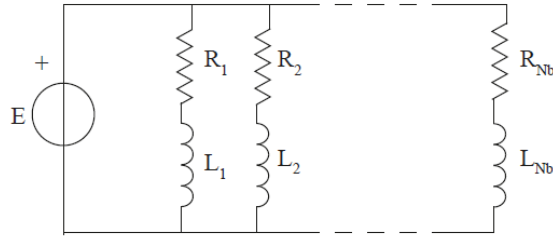


Figure 1.2: Lumped-parameter model

E , instead, represents the back-electromagnetic force on the track due to the time varying flux linkage λ generated by the PM array.

Using a reference frame fixed to the track, the permanent magnetic flux linkage λ can be rewritten using the complex notation; the lift and the drag forces are derived from the mechanical energy and following the steps illustrated by Galluzzi et al. [28], the levitation forces are formulated in equations 1.4 and 1.5 whose parameters description can be found in table 1.1.

$$F_{lift} = \frac{\Lambda_0^2}{\gamma} e^{\left(\frac{-2z_p}{\gamma}\right)} \sum_{k=1}^{N_b} \frac{\frac{\omega^2}{\omega_{p,k}^2}}{\left(1 + \frac{\omega^2}{\omega_{p,k}^2}\right)} \quad (1.4)$$

$$F_{drag} = \frac{\Lambda_0^2}{\gamma} e^{\left(\frac{-2z_p}{\gamma}\right)} \sum_{k=1}^{N_b} \frac{\frac{\omega}{\omega_{p,k}}}{\left(1 + \frac{\omega^2}{\omega_{p,k}^2}\right)} \quad (1.5)$$

Description	Formula	Measurement Unit
Magnet side length	a_m	mm
Number of magnets per pole pair	N_m	-
Pole pitch ratio	$\gamma = \frac{N_m a_m}{2\pi}$	-
Complex rotational velocity	$\omega = \frac{v}{r}$	rad/s
Natural frequency of each branches	$\omega_{p,k} = \frac{r_k}{L_k}$	rad/s
Flux linkage	Λ_0	Wb

Table 1.1: Levitation forces parameters

1.4 Thesis goal

The goal of this thesis is to analyse the experimental results using a test bench in terms of lift and drag force applied on a 90° Halbach array for different speeds and distances between the pad and the track. The test bench is in a laboratory scale but, through COMSOL Multiphysics® simulations the results are then rescaled. Afterwards, starting from the experimental data, using a multidomain approach and performing the root locus as proposed by Galluzzi et al. [28], a dynamic analysis is performed to find an optimal value of damping necessary to stabilise the system.

1.4.1 Outline

This work is organized as follows. In chapter 2 is illustrated the test bench and the quasi-static measurement system installed on it that will be used during the experiment; afterwards, the load cells attached on it are characterized in order to model any interference between the measurements in lift and drag direction.

In chapter 3 the aluminum disk and the copper rim of the test bench are characterized to see how far they deviated from the planarity. All these characterizations are made in order to better analyse the experimental results.

In chapter 4 the procedure to create a 90° Halbach array is illustrated and the related assembly on a pad. In addition, the non idealities sources also are taken into consideration.

Chapter 5 deals with the quasi-static experiment: after introducing the necessary instrumentation, the results are shown in terms of lift and drag curves. In chapter 6 the dynamic measurement system is illustrated and the choice of a voice coil as a damper is discussed; an attempt is made to characterise its most important quantities such as resistance, inductance, and intrinsic damping, which do not remain linear during its operation time; furthermore, the fitting analysis and the root locus are performed to evaluate the optimal damping necessary to stabilize the system. Finally, two possible control solutions that could be implemented on a dedicated control unit and on the test bench are illustrated.

At last, conclusion on the performed activities are drawn and proposal for further studies are provided.

Chapter 2

Test bench characterization

2.1 Main frame

In figure 2.1 a section view of the test bench main frame is represented: it is composed by a disk and a copper rim on it and a support steel structure that guarantees safety during the experiment. The disk is connected to a AKML74L Kollmorgen electric motor (datasheet on Ref [32]) that is used for propulsion through a torsional joint and a shaft. Figure 2.2 shows a photo of the real test bench layout.

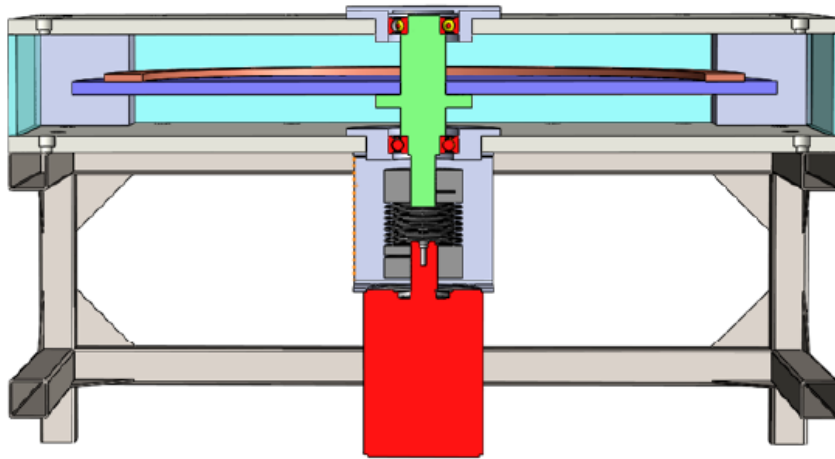


Figure 2.1: Test bench main frame drawing

2.2 Quasi-static measurement system

Figure 2.3 and figure 2.4 represent the drawing and the real measurement system used in the quasi-static experiment that is composed by the following



Figure 2.2: Real test bench layout

elements:

- *micrometric linear stage* (1) used to impose the distance between the copper rim and the PM array, that is the constant airgap z_p ;
- *load cells* (2, 6) used to measure the *lift* and *drag* forces; in particular, the load cells mounted in the experiment are HBM S2M type as shown in figure 2.5 (datasheet on Ref [33]);
- *magnetic pad* (4);
- *flexure hinges* (3,5) used to decouple the degrees of freedom within the measurement process.

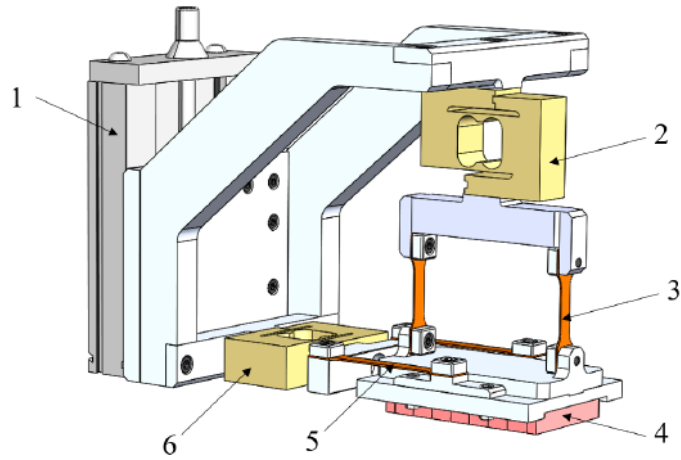


Figure 2.3: Quasi-static measurement system



Figure 2.4: Real quasi-static measurement system

2.3 Load cell characterization

2.3.1 Load cell framework

As said before, two load cells are used to measure lift and drag forces in two mutually perpendicular directions (figure 2.6).

The purpose of the characterization is to verify the accuracy of the load cell measurements and to model any interference between the measurements in the two directions of interest. A set consisting of ten sample masses (figure 2.7) whose mass is known with good accuracy (table 2.1), is used to perform the characterization.

First of all, the two load cells were characterised without being connected to any elements: they were loaded with 5 different masses and through a MGCplus amplifier (datasheet on Ref [34]) the true measured forces were

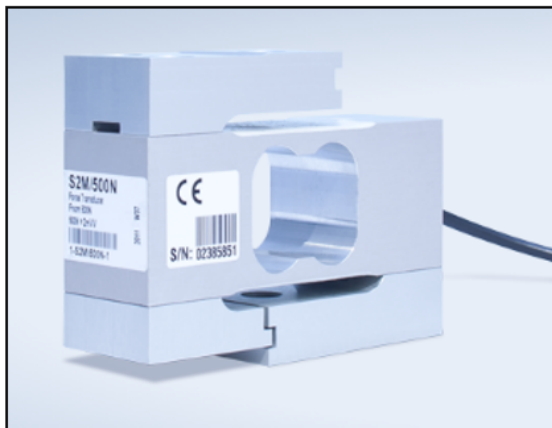


Figure 2.5: Load cell

Mass [Kg]	Q.ty	Weight force [N]
0.1300	1	1.27
0.3918	1	3.84
0.5300	1	5.19
0.6980	1	6.84
1.004	2	9.81
1.005	2	9.81
1.008	1	9.81
1.7610	1	17.26

Table 2.1: Sample masses parameters

quantified. Figure 2.8a and figure 2.8b shows the results: as we can see, the load cells measurements are very accurate, since the measured and the true forces are practically identical (the bisector represents the ideal behaviour of a load cell); also, the errors computed as the difference between the theoretical and measured values shown in the histograms in figure 2.9a and figure 2.9b are very small and they can be neglected.

2.3.2 Load cells interference modelling

Load cells 1 and 2 are positioned perpendicular to each other. This particular layout implies that by applying a force parallel to the lift direction even the cell that measures the force in the drag direction will be minimally affected by this force and will measure a value. The same observation also occurs vice versa, when a force is applied in the direction parallel to the drag. The situation just described represents an undesired effect and it is important to model it in order to evaluate its entity and possible corrections. During the acquisition procedure, load is applied in only one direction (lift or drag) and

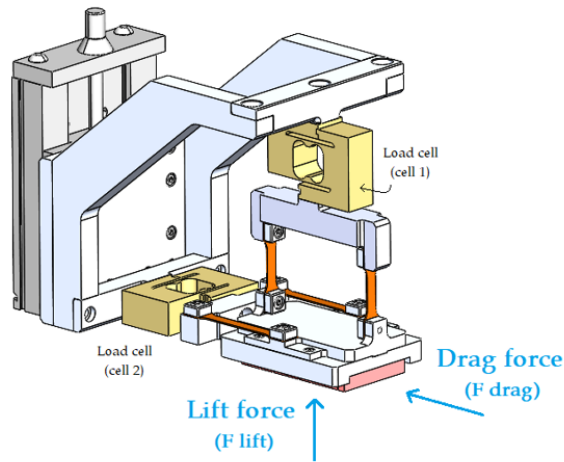


Figure 2.6: Load cell framework



Figure 2.7: Samples masses

measurements from both load cells are acquired. 17 different measurement points are defined with different combination of the sample masses in a range [0.1300 Kg – 5.0024 Kg]. In table 2.2 are shown the 17 different forces that will be applied to the loads cell.

Lift configuration

In the lift configuration, the force is applied only in the lift direction (measurement direction of cell 1); figure 2.10 shows how during the experiment the load cell is loaded: in particular, an aluminum plate was used to separate the sample masses made of ferromagnetic material and the Halbach array. Figure 2.11 illustrates the results: to performed a better analysis, the measurement points acquired on load cell 1 (in red) and load cell 2 (in blue) were interpolated using a *Curve Fitting* algorithm in MATLAB[®], from which we

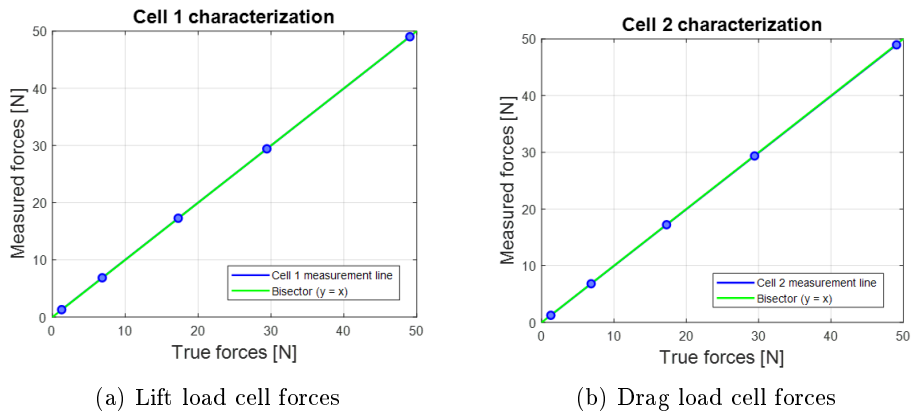


Figure 2.8: Load cells characterization

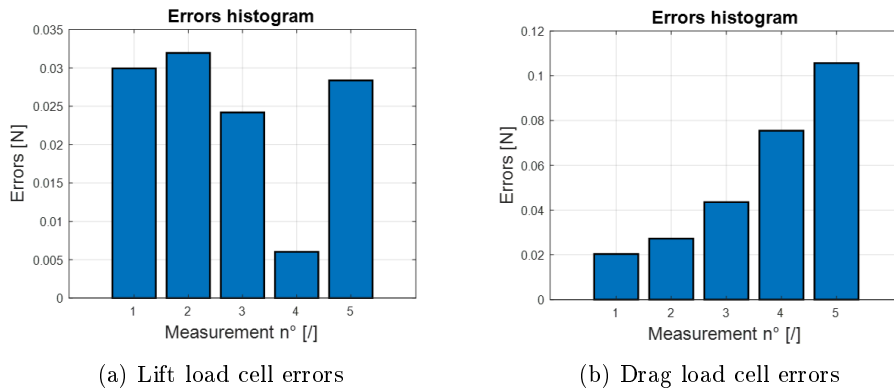


Figure 2.9: Load cells errors

obtain an angular coefficient (M) and an offset value (Q) both for the cell 1 and the cell 2 (table 2.3); these values are then used to plot two straight lines (figure 2.12): as expected, cell 1 curve follows the bisector while the cell 2 curve is almost always equal to 0, even if the zoom shows that also the load cell that measures the drag force is minimally affected by the forces applied only on the lift direction.

Moreover, the offset between the measured and the theoretical values that affects cell 1 can be plotted: as shown in figure 2.13, the maximum offset equal to 0.45 N is obtained when a force of 50 kg is applied and, since it represents less than 1 percent of the force, it can be neglected.

Drag configuration

In the drag configuration, the force is applied only in the drag direction (measurement direction of cell 2); figure 2.14 shows how during the exper-

1.27	3.84	5.19
8.11	9.81	13.65
17.26	19.62	23.46
26.46	29.43	33.27
36.27	39.24	43.08
46.70	49.05	

Table 2.2: Measurement point forces

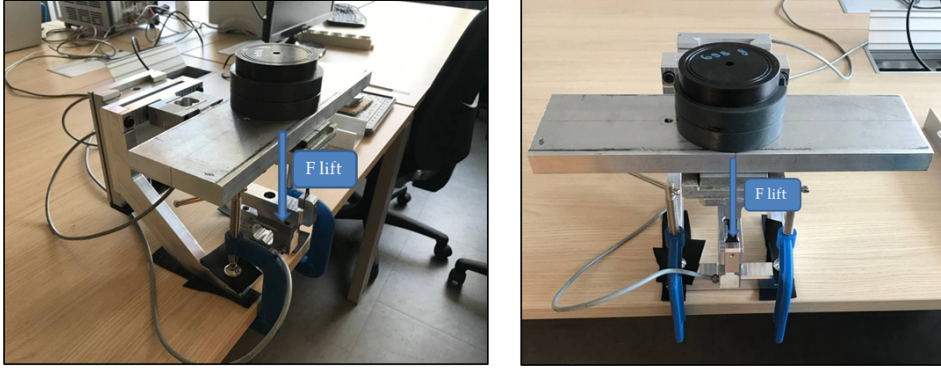


Figure 2.10: Lift configuration setup

iment the load cell is loaded. In figure 2.15 the results are represented: as in the previous case, to perform a better analysis, the measurement points acquired on load cell 1 (in red) and load cell 2 (in blue) were interpolated using a *Curve Fitting* algorithm in MATLAB[®], from which we obtain an angular coefficient (M) and an offset value (Q) both for the cell 1 and the cell 2 (table 2.4); these values are then used to plot two straight lines (figure 2.16): as expected, cell 2 curve follows the bisector while the cell 1 curve is almost always equal to 0, even if the zoom shows, as in the previous configuration, that also the load cell that measures the lift force is affected by the forces applied only on the drag direction; the offsets of cell 2 can be neglected since the maximum one is equal to 0.11 N and represents the 0.23 percent of 46 kg (figure 2.17).

Interference matrix

It is possible to numerically compute the interference that the two cells exert on each other (equation 2.1 and equation 2.2).

$$y_1 = M_{1,1}x_l + M_{1,2}x_d + Q_{1lift} + Q_{1drag} = M_{1,1}x_l + M_{1,2}x_d + Q_{1,1} \quad (2.1)$$

$$y_2 = M_{2,1}x_l + M_{2,2}x_d + Q_{2lift} + Q_{2drag} = M_{2,1}x_l + M_{2,2}x_d + Q_{2,1} \quad (2.2)$$

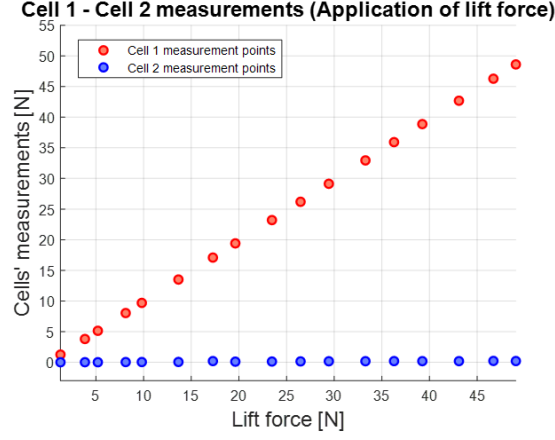


Figure 2.11: Lift configuration measurements

	Angular coefficient	Offset value
Cell 1	$M_{1lift} = 0.9912$	$Q_{1lift} = -0.0241$
Cell 2	$M_{2lift} = 0.004589$	$Q_{2lift} = 0.009415$

Table 2.3: Lift configuration angular coefficients and offsets

The force measured in the lift direction y_1 (measured by the load cell 1) is the sum of three different contributions: a contribution due to the force applied along the lift direction x_l , a contribution due to the force applied along the drag direction x_d and a contribution due to the offsets of the lines interpolating the measurement points (and related to the load cell 1), which add up to a single offset coefficient $Q_{1,1}$ (equation 2.1).

Similar reasoning can be applied regarding the force measured along the drag direction y_2 (by the load cell 2) (equation 2.2).

The previous equations can be rearranged in matrix form:

$$\begin{bmatrix} y_1 \\ y_2 \end{bmatrix} = \begin{bmatrix} M_{1,1} & M_{1,2} \\ M_{2,1} & M_{2,2} \end{bmatrix} \begin{bmatrix} x_l \\ x_d \end{bmatrix} + \begin{bmatrix} Q_{1,1} \\ Q_{2,1} \end{bmatrix} \quad (2.3)$$

$$Y = MX + Q \quad (2.4)$$

where:

- Y is a $[2 \times 1]$ matrix that represents the forces measured on load cell 1 (y_1) and load cell 2 (y_2);
- X is a $[2 \times 1]$ matrix represents the theoretical forces that are applied on load cell 1 (x_l) and load cell 2 (x_d).
- M is a $[2 \times 2]$ matrix that contains the angular coefficients of the lines interpolating the measurement points.

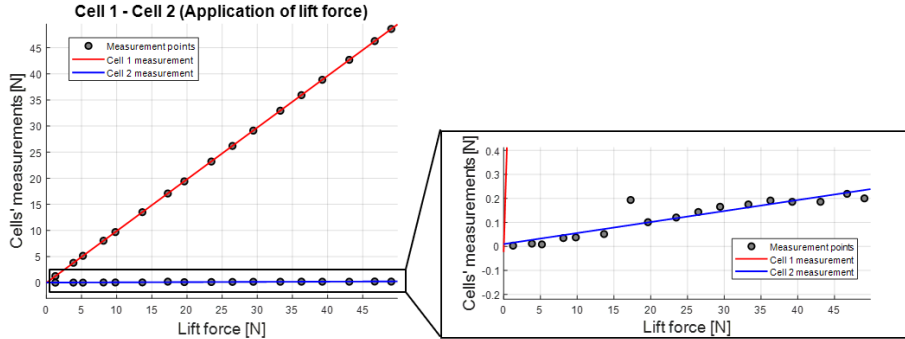


Figure 2.12: Lift configuration measurement fitting

	Angular coefficient	Offset value
Cell 1	$M1_{drag} = 0.00283$	$Q1_{drag} = 0.01080$
Cell 2	$M2_{drag} = 1.0010$	$Q2_{drag} = 0.02321$

Table 2.4: Drag configuration angular coefficients and offsets

- Q is a [2 x 1] matrix that contains the offsets of the lines interpolating the measurement points.

By inverting equation 2.3, it is possible to derive the real applied forces x_l and x_d from the values of the forces measured in the two directions (lift and drag) (equation 2.5):

$$\begin{bmatrix} x_l \\ x_d \end{bmatrix} = \begin{bmatrix} M_{1,1} & M_{1,2} \\ M_{2,1} & M_{2,2} \end{bmatrix}^{-1} \left(\begin{bmatrix} y_1 \\ y_2 \end{bmatrix} - \begin{bmatrix} Q_{1,1} \\ Q_{2,1} \end{bmatrix} \right) \quad (2.5)$$

Using MATLAB[®], the numerical results can be computed (equations 2.6 and 2.7):

$$\begin{bmatrix} M_{1,1} & M_{1,2} \\ M_{2,1} & M_{2,2} \end{bmatrix} = \begin{bmatrix} 0.9912 & 0.0028 \\ 0.0046 & 1.0010 \end{bmatrix} \quad (2.6)$$

$$\begin{bmatrix} Q_{1,1} \\ Q_{2,1} \end{bmatrix} = \begin{bmatrix} -0.0133 \\ 0.0326 \end{bmatrix} \quad (2.7)$$

Measurement correction

Using equation 2.5, the force values measured by the load cell can be corrected finding the real applied forces; in this way, when a force is applied in the drag direction, the value measured by the lift load cell will be even more equal to zero and viceversa. If we analyse figure 2.18a that shows the drag

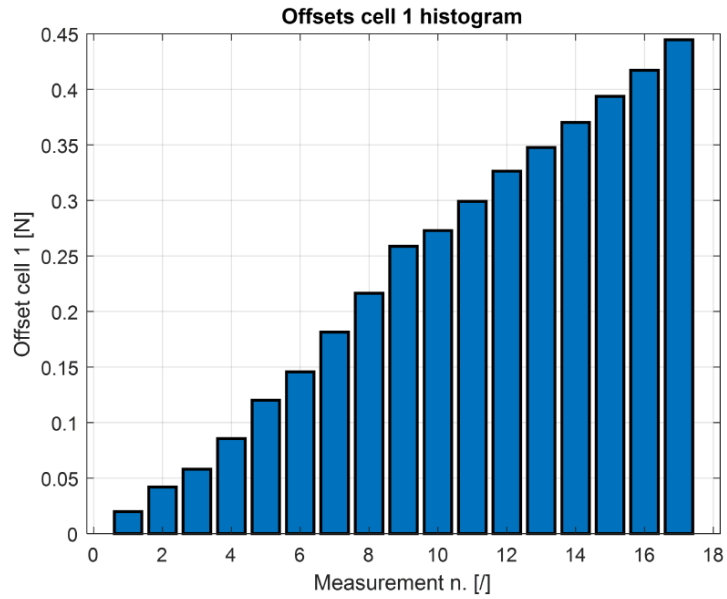


Figure 2.13: Cell 1 offsets vs the applied forces in the lift direction

configuration results, the orange line represents the theoretical values that cell 1 should measure (null in this case): the green line, instead, represents the force values obtained after the correction. If we compare this line with the black points that represents the measured values, after the correction they are closer to 0. This is highlighted in figure 2.18b that shows the errors that affect cell 1 in the drag configuration: they decrease after the correction.

Same analysis can be done for the lift configuration regarding cell 2 (figure 2.19a and figure 2.19b).



Figure 2.14: Drag configuration setup

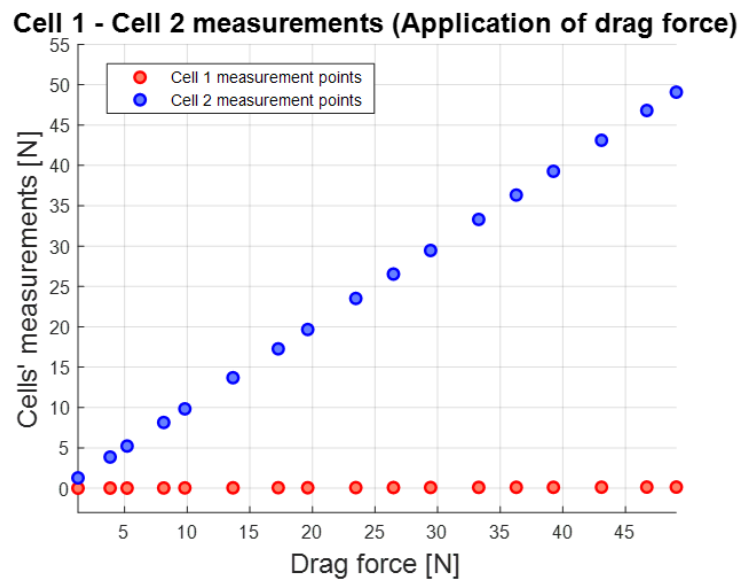


Figure 2.15: Drag configuration measurements

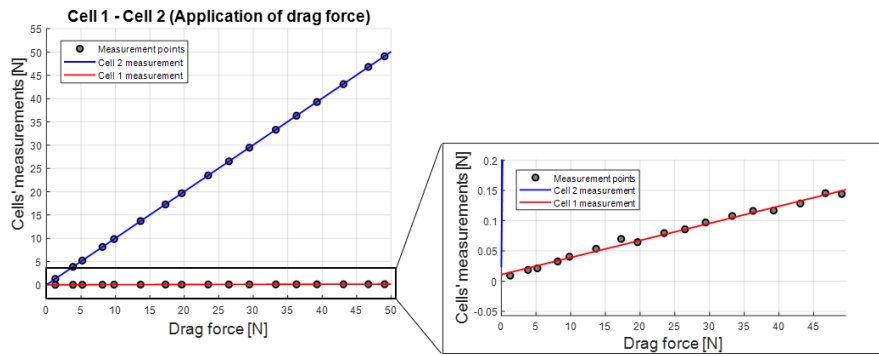


Figure 2.16: Drag configuration measurement fitting

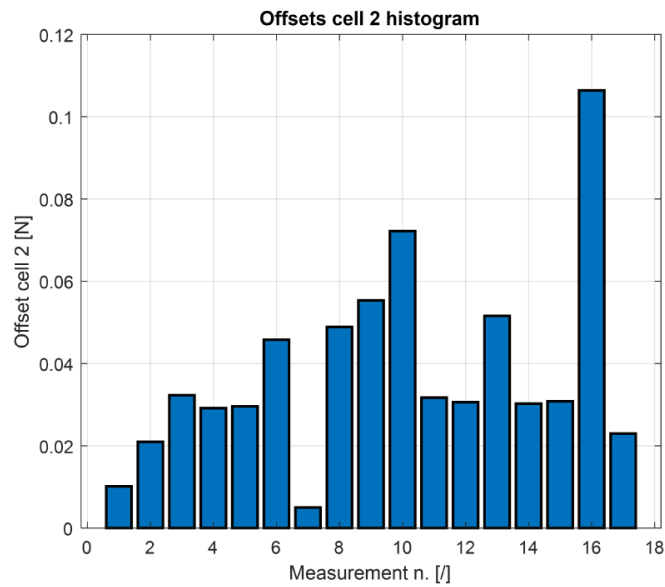
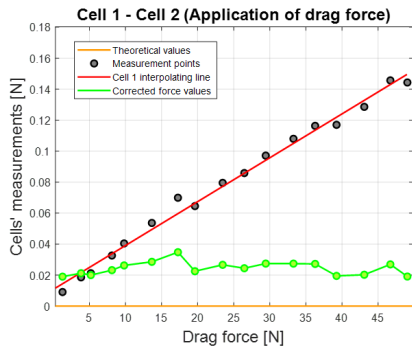
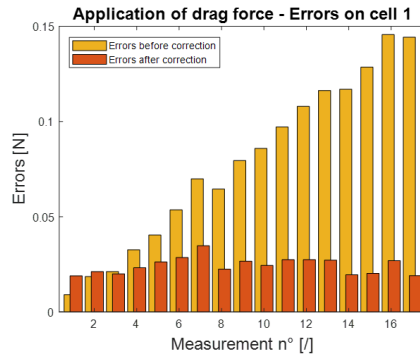


Figure 2.17: Cell 2 offsets vs the applied forces on drag direction

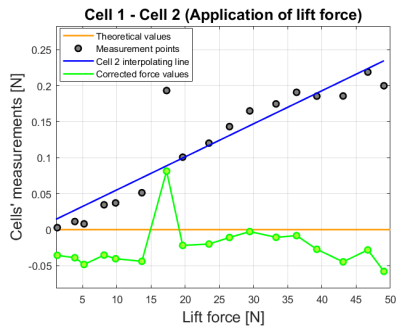


(a) Drag configuration results

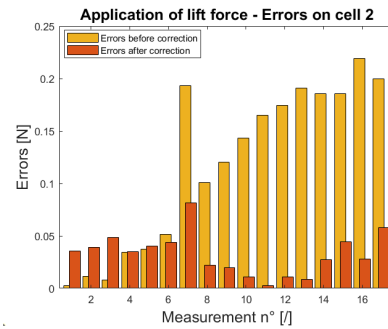


(b) Magnitude errors

Figure 2.18: Drag configuration results and magnitude errors on cell 1 before and after the correction



(a) Lift configuration results



(b) Magnitude errors

Figure 2.19: Drag configuration results and magnitude errors on cell 2 before and after the correction

Chapter 3

Aluminum disk and copper rim characterization

In order to analyse the data as best as possible, the aluminum disk and the copper rim were characterised to see how far they deviated from the planarity. The measurements were performed using a Vogel digital dial indicator (or centesimal dial gauge) (figure 3.1 and datasheet on Ref [35]).



Figure 3.1: Vogel digital dial indicator

3.1 Aluminum rotor height measurement

As shown in figure 3.2, the digital dial indicator was fixed to the frame structure through a piece of wood and two C-clamps while the terminal part touched the disk measuring the different heights.

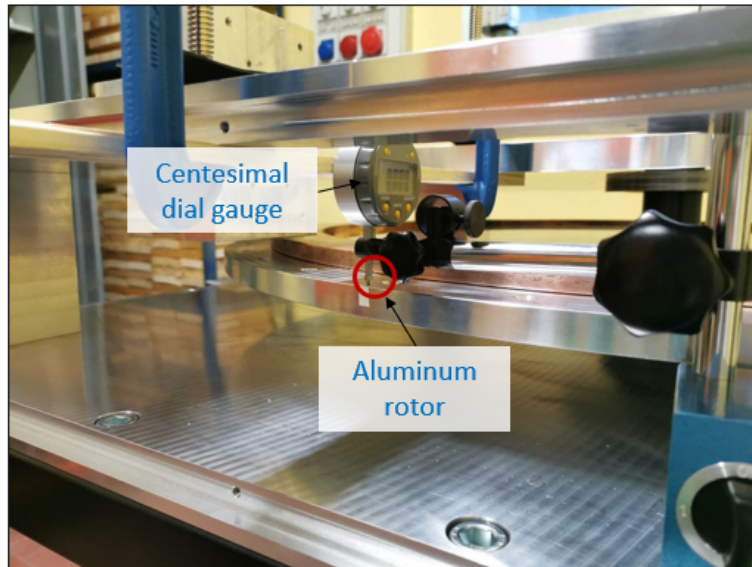


Figure 3.2: Aluminum rotor height measurements setup

After turning the rotor through 360 degrees, the results in figure 3.3 were obtained: as we can see, there is a peak of 0.5 mm in a portion of the disk, while the other part is almost planar.

3.2 Copper rim height measurement

In order to proceed to the copper rim height measurements, the digital dial comparator was fixed to the frame structure as the previous case (figure 3.4).

Measurements were performed in 5 different points of the rim, separated from each other by 10 mm (figure 3.5). The obtained qualitative trend is shown in figure 3.6 and figure 3.7: the trend of the track is very irregular, achieving peaks of 0.3 to -0.5. In particular, the minimums of each measurement are at a specific point on the track, i.e. where the start and end ends of the copper profile have been welded together to create the copper rim (figure 3.8).

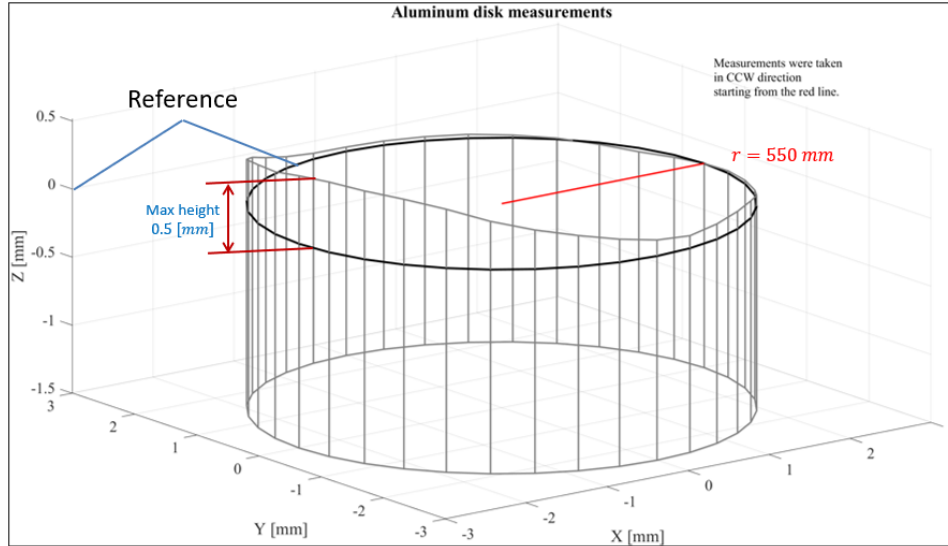


Figure 3.3: Aluminum rotor measurement results

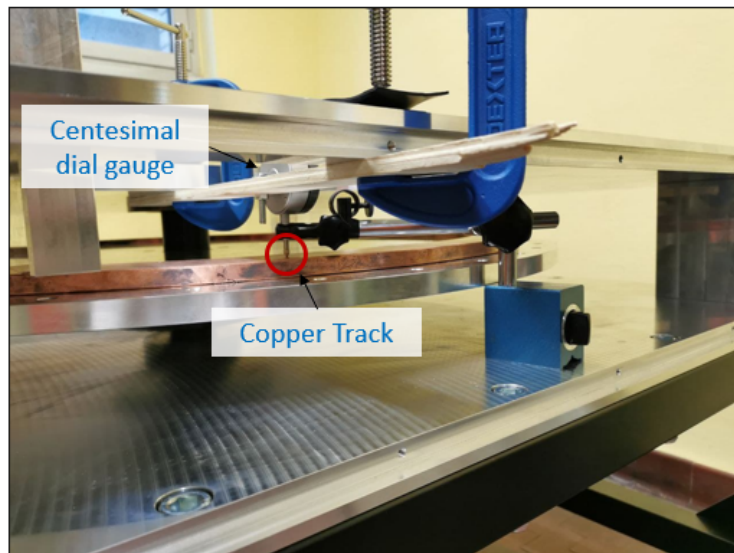


Figure 3.4: Copper rim height measurements setup

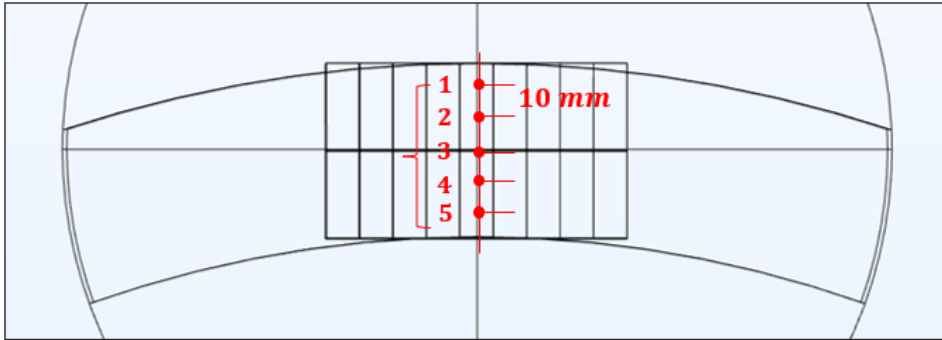


Figure 3.5: Copper rim measurement points

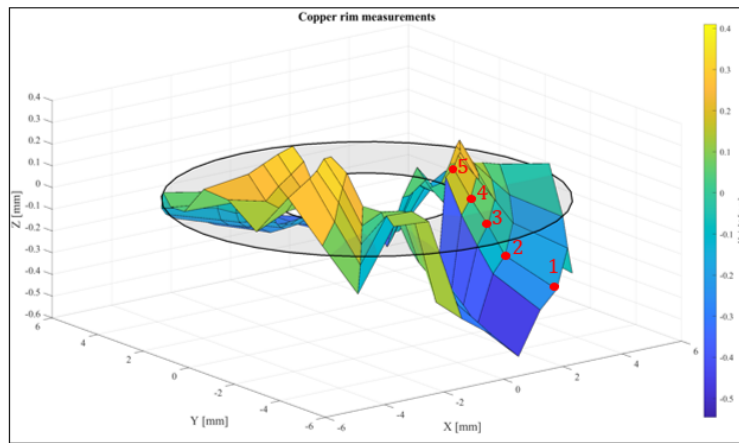


Figure 3.6: a) Qualitative trend of the copper rim: 3D analysis

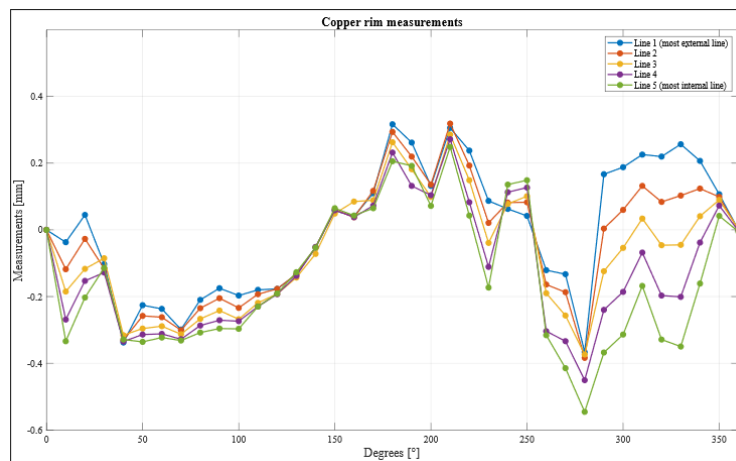


Figure 3.7: b) Qualitative trend of the copper rim: 2D analysis



Figure 3.8: Copper rim defect

Chapter 4

Halbach array

An Halbach Array is a particular union, or layout, of permanent magnets arranged in such a way as to strengthen the magnetic field along one face of the array while at the same time cancelling out the magnetic field in the opposite face by interference.

The quasi-static experiment were performed with two different configurations of Halbach arrays that differ from each other by the direction of polaritation of the magnets that composed them: the 90° configuration and the 45° configuration.

Figure 4.1a shows the general scheme of the 90° configuration Halbach array: the polaritation of each magnets is perpendicular with respect to the one of the magnets next to it, following a precise order.

Figure 4.1b, instead, shows the general scheme of the 45° configuration Halbach array: in this case, the polaritation of each magnet is at 45° with respect to the one of the magnets next to it with a precise order.

In the following sections, only the 90° configuration will be considered and it will be illustrated the procedure for creating the Halbach array and the obtained results.

Other important informations which can be anticipated and will be used for the fitting analysis in section 6.2 are the number of magnets per pole pair N_m equal to 4 and the magnet side length a_m equal to 12 mm.

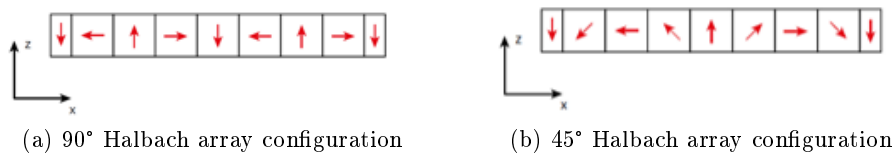


Figure 4.1: Halbach array configurations

4.1 Halbach array single assembly procedure

In this section the procedure to create a single Halbach array will be illustrated. The material required is as follows:

- 9 magnets measuring 30x12x12 mm (the properties are reported in figure 4.2);
- one steel plate (figure 4.3a);
- one plate of non-ferromagnetic material (e.g. aluminium) (figure 4.3a);
- three plastic plates of different sizes (figure 4.3b);
- wooden profiles (useful for handling and positioning the magnets) (figure 4.3c);
- hammer;
- clamp (figure 4.3d);
- two-component glue UHU Plus Endfest 300 kg (datasheet on Ref [36]);
- double-sided adhesive tape.

1. Technical information

Article ID	Q-30-12-12-Z
EAN	7640155439855
Material	NdFeB
Shape	Block
Size	30 x 12 x 12 mm
Side 1	30 mm
Side 2	12 mm
Side 3	12 mm
Pole faces	30 x 12 mm
Tolerance	+/- 0,1 mm
Direction of magnetisation	Axis 12 mm
Coating	Zinc-plated (Zn)
Manufacturing method	sintered
Magnetisation	N52
Strength	approx. 9,4 kg (approx. 92,2 N)
Displacement force	approx. 1,9 kg (approx. 18,4 N)
Max. working temperature	65°C
Weight	32,8320 g
Curie temperature	310 °C
Residual magnetism Br	14200-14700 G, 1,42-1,47 T
Coercive field strength bHc	10,8-12,5 kOe, 860-995 kA/m
Coercive field strength iHc	≥12 kOe, ≥955 kA/m
Energy product (BxH)max	48-53 MGOe, 380-422 kJ/m ³

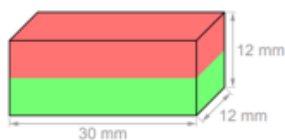
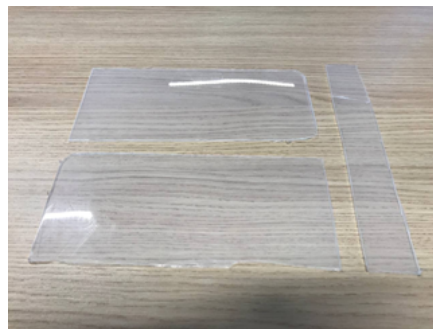


Figure 4.2: Magnets properties

The magnets have the same dimensions so therefore the two magnets with one side of the cross-section halved (located at the extremes of the configuration as in figure 4.1a) will not be present.



(a) Aluminum plate (above) and steel plate (below)



(b) Plastic plates



(c) Wooden profiles



(d) Clamp

Figure 4.3: Materials for a single Halbach array

The following steps are the operating procedure for creating a single Halbach array:

- glue the plastic plates onto the steel and aluminium plates using double-sided adhesive tape so that the configuration is similar to the one shown in figure 4.4;

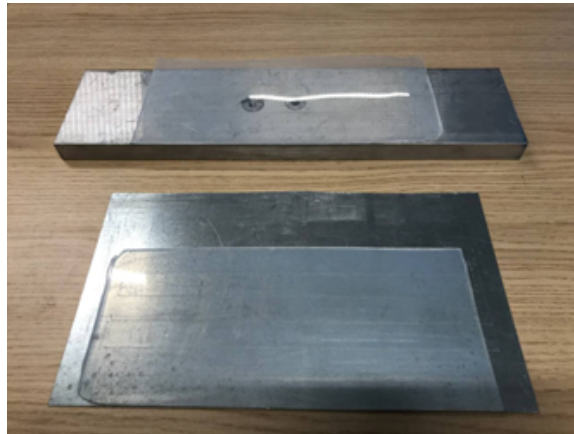


Figure 4.4: Single Halbach array assembly procedure: step 1

- position the metal plate fixed with the plastic plates and the third and last plastic plate inside the clamp in such a way as to form a configuration that allows the magnets to be inserted and held in position. The configuration is shown in figure 4.5 (the clamp is not the one used in reality but only a representation of it).

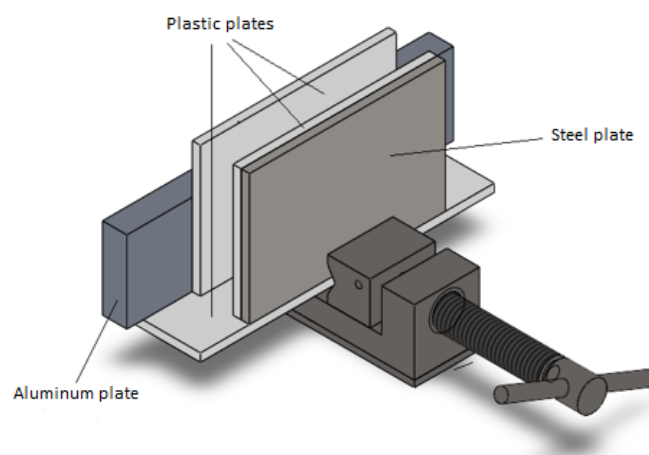
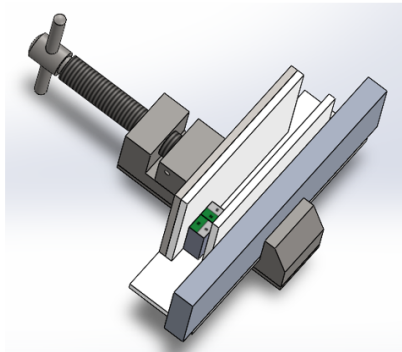


Figure 4.5: Single Halbach array assembly procedure: step 2



(a) SOLIDWORKS assembly model



(b) Real assembly photo

Figure 4.6: Single Halbach array assembly

- insert the magnets one at a time, taking care to place them in the correct position and helping with this with the wooden profiles. Before positioning the magnets, spread a layer of two-component glue on the face that will be in contact with other magnets. After positioning, from the second magnet onwards, adhere the surfaces of the magnets in contact by repeatedly tapping with the wooden profiles and a hammer. The configuration obtained should be similar as shown in figures 4.6a and 4.6b.
- repeat the previous step until all the magnets are fully inserted. Then let the two-component glue rest for at least 24 hours before releasing the Halbach array from the clamp. The optimal situation would be to heat the whole assembly to a temperature of 70 degrees Celsius so that the glue solidifies in a much shorter time and maximum holding power is obtained from it.
- clean the Halbach array of external plastic and glue residues. The final result is shown in figure 4.7 (the green lines indicates the direction of polaritation of each magnets as in the scheme in figure 4.1a).



Figure 4.7: Single Halbach array

4.2 Halbach arrays assembly procedure

This section illustrates how to assemble two single Halbach arrays created following the above procedure, in order to create the Halbach array with the dimension needed in the experiment; the material required is as follows:

- 2 complete Halbach arrays (dimensions 30x12x108);
- 2 aluminium L-profiles;
- 6 plastic plates;
- clamp;
- two-component glue UHU Plus Endfest 300 kg (datasheet on Ref [36]).

The operating procedure is the following one:

- glue the plastic plates to the two aluminium profiles so that they form a complete covering. This is necessary to ensure that the glue does not come into direct contact with the aluminium and thus make it difficult to separate the two Halbach arrays once the procedure is complete;
- carefully lay the two Halbach arrays on the plastic-coated L-profiles as shown in the figure 4.8;
- place the assemblies obtained on the clamp, taking care to place them at a sufficiently large distance so that the repulsion forces between the two Halbach arrays do not interfere with the process and do not result in displacement of the arrays. The clamp that is used must be made of ferromagnetic material so that an attractive force is established in the direction normal to the surface of the Halbach arrays to ensure that they remain in position during the process (figure 4.9);

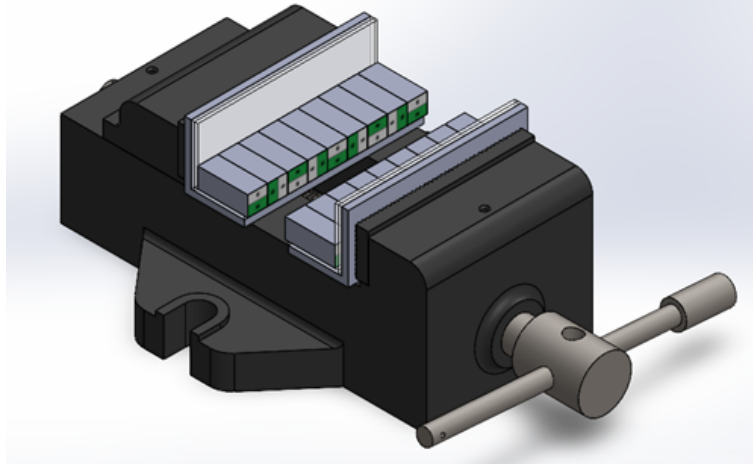
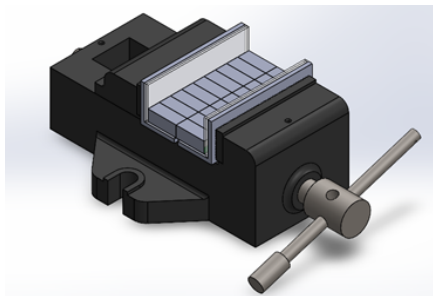


Figure 4.9: Halbach array assembly procedure: step 3



(a) SOLIDWORKS assembly model



(b) Real assembly photo

Figure 4.10: Halbach array assembly

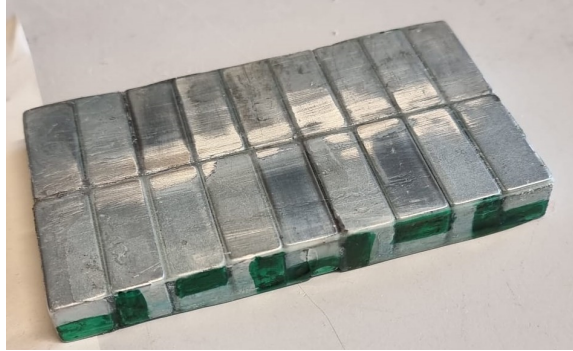


Figure 4.11: Halbach array

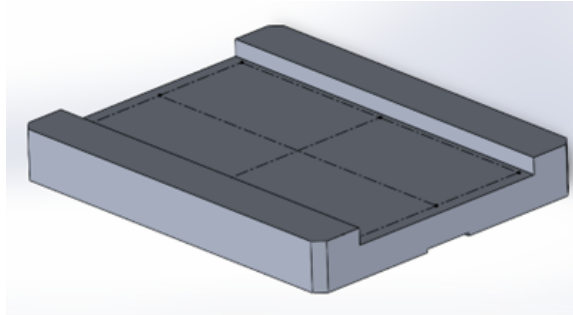


Figure 4.12: Halbach array assembly on a pad: step 1

- apply two-component glue to the face of the array that is to be glued and place the array on the aluminium pad (figure 4.13). During this step, it is important that the support planes are perfectly flat in order to ensure the stability of the array and avoid slippage that would lead to incorrect centring. If you have the possibility, heat the assembly in an oven at a temperature of 70 degrees Celsius for 45 minutes, otherwise leave it to rest for at least 24 hours before handling the assembly. The final result is shown in figure 4.14.

4.4 Non idealities sources

To test the quality of the above created pad, some possible non idealities sources that could affected the measurements in the quasi-static experiment should be investigated.

Magnetic Flux density B_y comparison

In figure 4.15a is shown the comparison between the experimental measurements of the magnetic flux density B_y carried by a gaussmeter with a



Figure 4.13: Halbach array assembly on a pad: step 2



Figure 4.14: Final pad

transversal probe at a distance equal to 0.75 mm (figure 4.15b) (black line) and the COMSOL simulation calculated at the same distance (red line): the experimental data follow the simulations quite accurately.

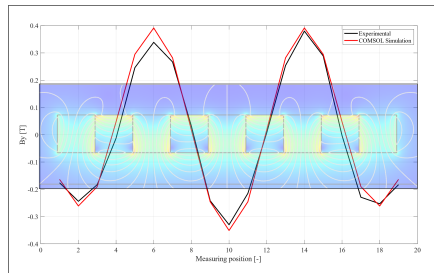
Pad inclination wrt copper rim track

Mounted on its experimental configuration, the pad is not perfectly aligned with respect to the copper rim, so the yaw, roll and pitch angle of the pad has been evaluated experimentally and subsequently included in the 3D COMSOL model simulation (figure 4.16).

Other non idealities source

Other possible non idealities sources are listed below:

- eddy current end edge effects could not be negligible;



(a) Magnetic flux Comparison



(b) Experimental measurements

Figure 4.15: Magnetic flux density comparison

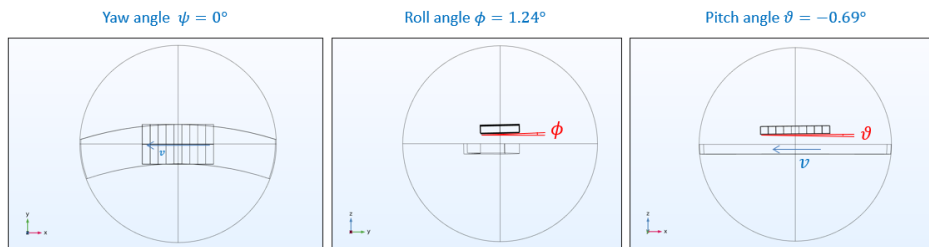


Figure 4.16: Yaw, roll and pitch angle

- there could be air gap uncertainty due to pad vibrations, copper rim not rectified and aluminum rotor not balanced (as shown in section 3.1).

Chapter 5

Quasi-static experiment

The goal of the quasi-static experiment is to obtain lift and drag curves for different air gaps (distances between pad and copper rim) and different angular velocities of the disk. Figure 5.1 shows schematically the procedure followed during the test.

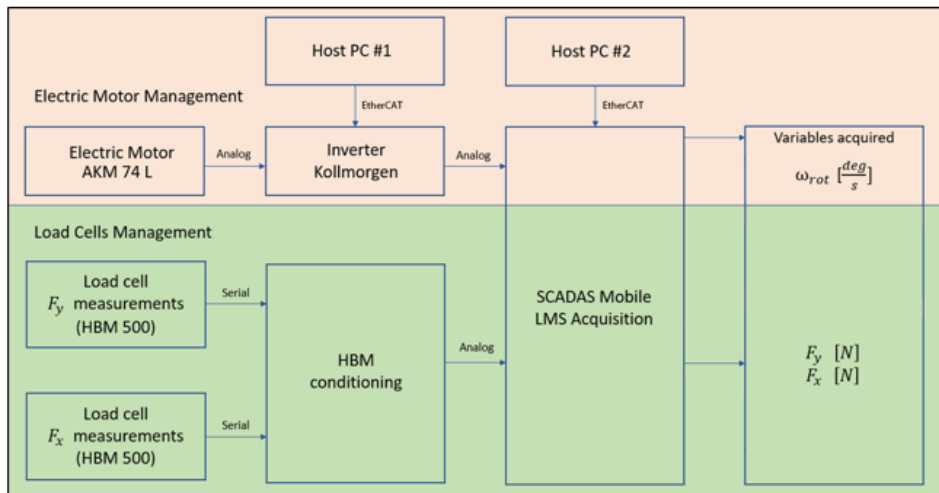


Figure 5.1: Quasi-static acquisition procedure

An host PC, using the KollMorgen Workbench, controls the electric motor through an inverter setting its velocity to a desired value. Another host PC is connected to the SCADAS Mobile LMS (datasheet on Ref [37]) that acquires the variables of interest, such as the motor angular velocity ω_{rot} [$\frac{deg}{s}$], obtained directly from the inverter, the *lift* and *drag* forces obtained by the load cells (HBM 500) mounted in the experiment. Figure 5.2 shows a photo of the instrumentation setup above described.

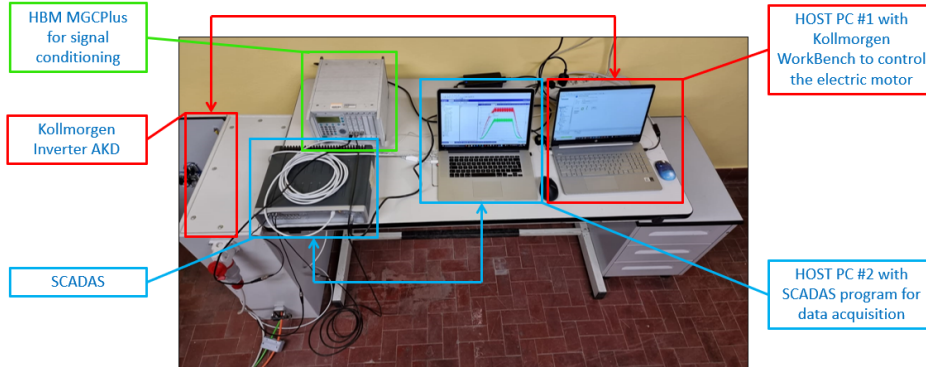


Figure 5.2: Quasi-static acquisition setup

5.1 Instrumentation set-up

Electric motor management

Considering the inverter (figure 5.3a), from the connector X8 (pin 8 of the inverter), it is possible to read the filtered velocity of the disk (± 10 V analog signal). Using two crocodile probes with BNC connector and considering that pin 7 of the connector X8 is used as ground, the analog information is sent to the SCADAS for acquisition (figure 5.3b).

Kollmorgen WorkBench setup

It is necessary to convert the motor speed into an analog signal (± 10 V) by setting a gain via the Kollmorgen WorkBench interface: to calculate it, we have to start from the maximum speed assumed to be reached during the tests: in the considered experiment, assuming a maximum speed of 500 rpm, we have added 20 percent to it reaching 600 rpm. After that, considering only the positive range of the analog signal, the conversion becomes:

$$\frac{600}{10} = 60 \left[\frac{rpm}{V} \right] \quad (5.1)$$

Then, $\frac{rpm}{V}$ must be converted in $\frac{deg}{s}$ multiplying the value in equation 5.1 by 6. So the final gain to set is $360 \frac{deg}{s}$ (figure 5.4a).

Via the "Service Motion" interface of the Kollmorgen WorkBench it is possible to set the desired acceleration and deceleration value and the desired reference speed to be reached during the test. In order to start the test, the "Start" button must be pressed and the disk will accelerate eventually reaching the desired reference speed. After that, when the speed has stabilised, by clicking on "Axis disable" button, it is possible to cut the power to the

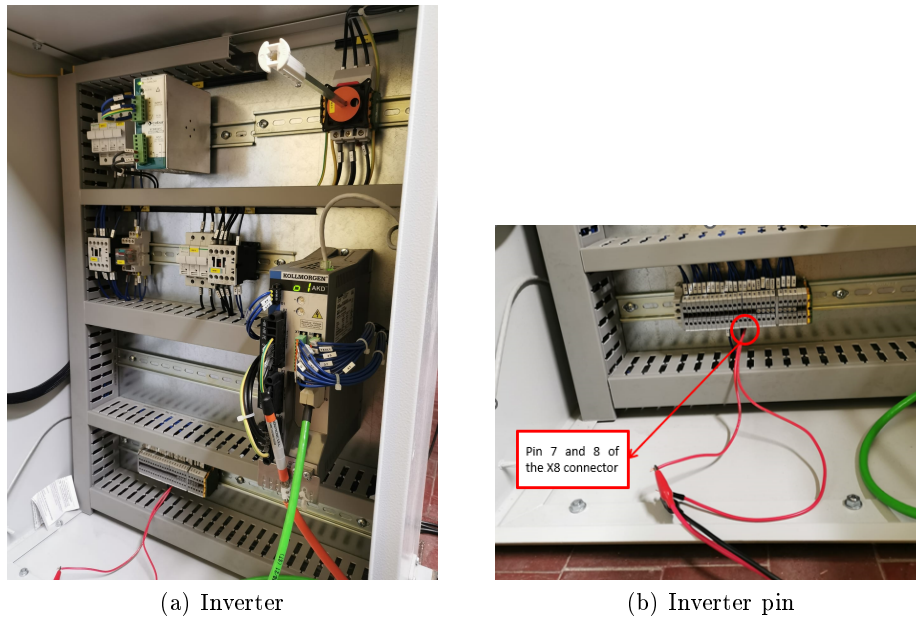


Figure 5.3: Electric motor management

motor by putting it in "neutral" state and let the disk brake due to friction drag and inertia losses (figure 5.4b).

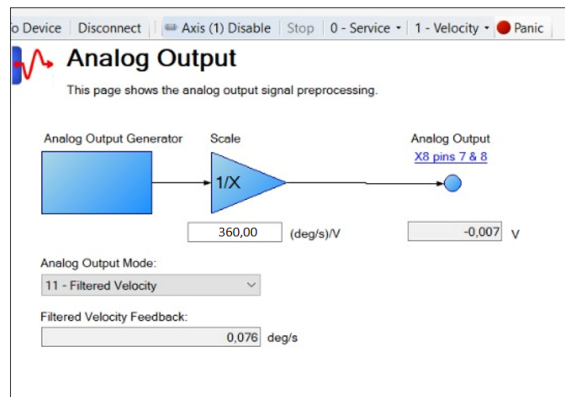
SCADAS setup

Figure 5.5a shows the "Channel Setup" window of the SCADAS interface that shows the three important data to be obtained during the experiment. Input 1 and input 2 are the lift and drag force signals measured by the load cells, respectively: these signals are conditioned by HBM MGCPlus and sent to SCADAS as analog signals. Input 3, instead, is the angular velocity obtained from the inverter: since it is an analog signal (± 10 V), it must be converted using the previously calculated gain setting an "actual sensitivity" calculated as in equation 5.2.

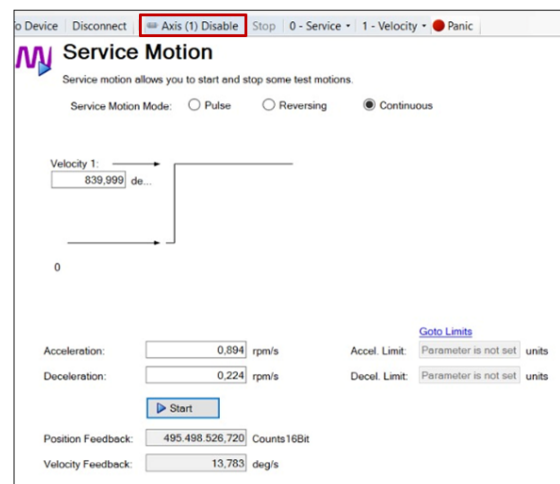
$$\frac{1}{(GAIN_{Kollmorgen})} = \frac{1}{360} = 2.78e - 3 \frac{V}{\frac{deg}{s}} \quad (5.2)$$

Also in "Channel Setup", the "actual sensitivity" of the lift and drag force channels are to be set equal to 20 mV (the load cells, in fact, have a nominal sensitivity equal to 2 mV/V which must be multiplied by 10 V that is the signal output range).

In addition, in "Acquisition Set-up", it must be set an "EU Range" for all channels that is proportional to the force and speed values expected from the test, otherwise "Overload" will occur during acquisition (figure 5.5b).



(a) Kollmorgen Workbench gain setup



(b) Kollmorgen WorkBench service motion setup

Figure 5.4: Kollmorgen WorkBench setup

5.2 Experimental results

5.2.1 Time behaviour

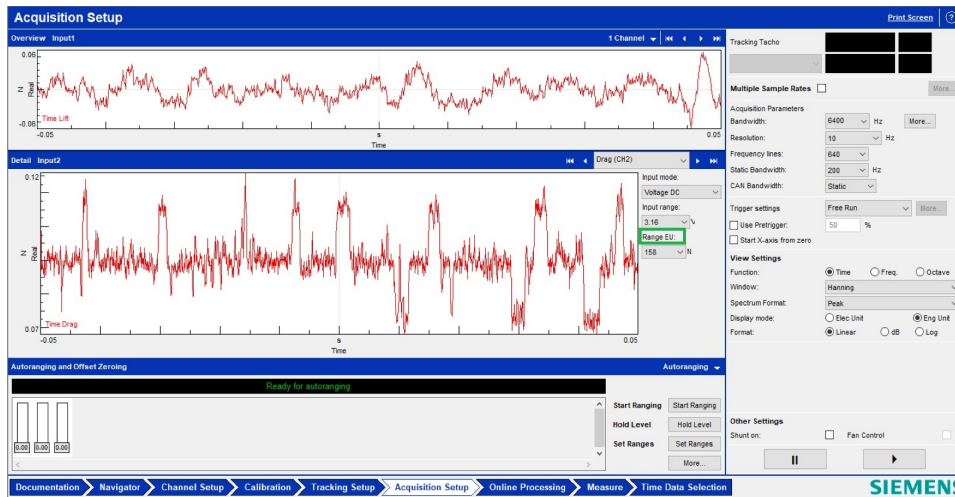
Quasi-static test have been performed at ω_{ref} equal to 400 rpm: figure 5.6a shows the acquired behaviours of ω_{rot} at different air gaps (experimental tests were conducted for 9 different air gaps shown in figure 5.6b).

The data acquisition consists of three phases:

- the first one is the *acceleration phase* during which the disk reaches the velocity set via Kollmorgen WorkBench;
- the second one is the *steady-state speed phase* during which the disk have reached the set velocity, so the motor keeps it constant;

Physical Channel	On/Off	Channel Group	Point	Direction	Input mode	Coupling	Measured Quantity	Electrical Unit	Actual Sensibility	FrontEnd Weighting	Pre-weighting	Pre-gain1	Pre-gain2
1	<input type="checkbox"/>	Tacho	Tacho	None	Voltage DC	Single Ended							
2	<input type="checkbox"/>	Tacho	TachoFlyw	None	Voltage DC	Single Ended							
3	<input checked="" type="checkbox"/>	Vibration	Lift	None	Voltage DC	Single Ended	Force	mV	20 mV/N	Linear	Linear	1	1
4	<input checked="" type="checkbox"/>	Vibration	Drag	None	Voltage DC	Single Ended	Force	mV	20 mV/N	Linear	Linear	1	1
5	<input checked="" type="checkbox"/>	Vibration	Angular Velocity	None	Voltage DC	Single Ended	Angular Velocity	V	0.00278 V/(°/s)	Linear	Linear	1	1

(a) SCADAS channel set up



(b) SCADAS acquisition set up

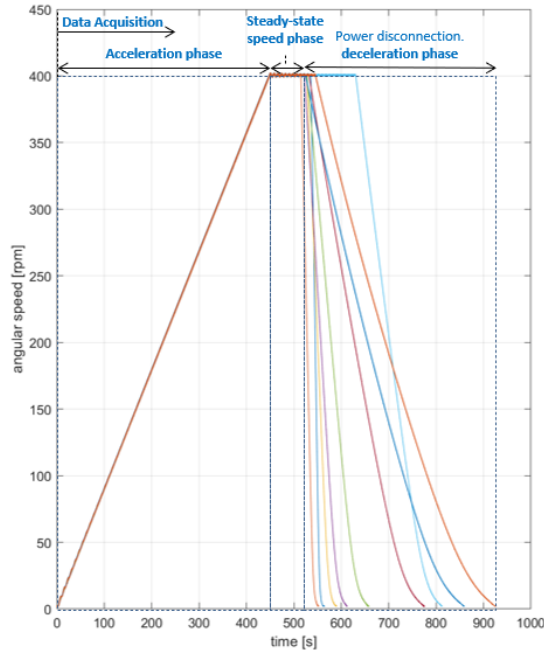
Figure 5.5: SCADAS setup

- the third is the *deceleration phase* in which the power is disconnected so the velocity disk starts to decrease until it reaches zero: interestingly, the smaller the gap, the faster the disc decelerates, resulting in increasingly steep deceleration curves.

Even more interesting are the curves in figure 5.7a and figure 5.7b that show the time behaviours of lift and drag forces for the 9 experimental tests.

Regarding the magnitude, both for the drag and the lift force, it is inversely proportional to the air gap: so smaller air gaps produce higher values of forces.

Regarding the trend of the forces, when the power is disconnected, the lift force immediately decreases following a curve that is steeper the smaller the air gaps are; instead the drag curves show a slightly different trend: the force reaches its maximum value at the electromagnetic pole (3D FEM simulations in COMSOL Multiphysics[®] show an electromagnetic pole at 163 rpm) then decreases reaching the steady value; when the power is disconnected, there is a peak of the force that reaches almost the value before the electromagnetic pole and then decreases until zero as the lift force.



(a) Quasi-static time behaviour results



(b) Air gaps legend

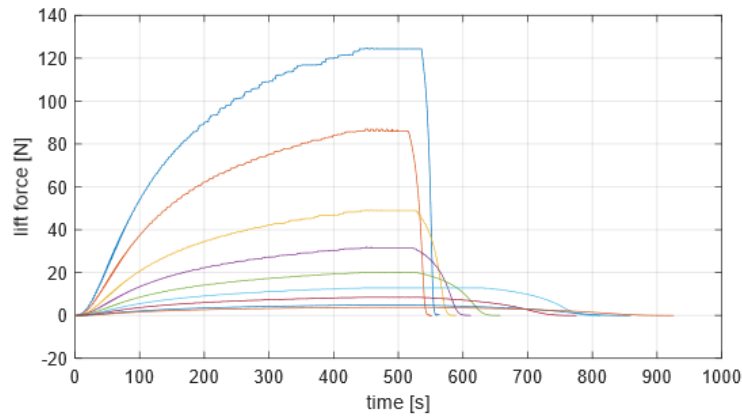
Figure 5.6: Quasi-static time response

5.2.2 Speed behaviour

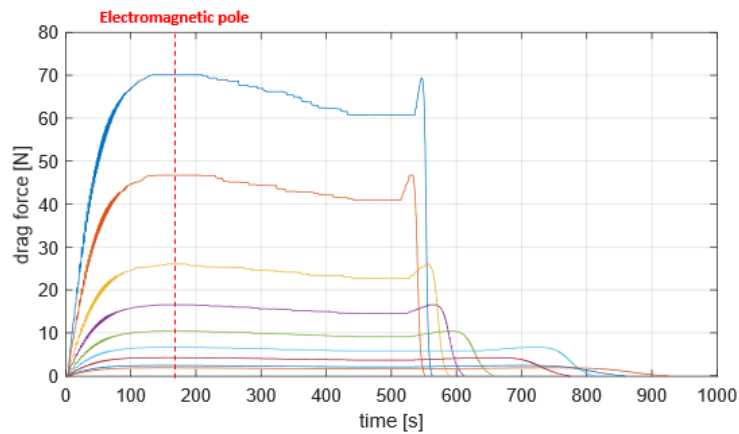
It is interesting to plot the speed behaviour of the drag and lift forces during the deceleration phase (figure 5.8a and figure 5.8b): here too, it can be clearly seen that magnitude force increases with small gaps and the trend of the drag force before and after the electromagnetic pole.

5.2.3 Uncertainty zone

In section 4.4 was described the inclination and orientation of the pad with respect to the copper rim considering them as a possible source of non idealities. Using COMSOL Multiphysics[®] is possible to draw an uncertainty zone due to this phenomenon on the lift and drag curve as shown in figure 5.9: the *upper bound* represents the nominal pad set up, so the values of forces of the pad if it were not tilted, while the *lower bound* represents the tilted pad set up. It is important to notice that the *experimental data* lies within the numerical results' bounds.



(a) Lift forces time behaviour



(b) Drag Forces time behaviour

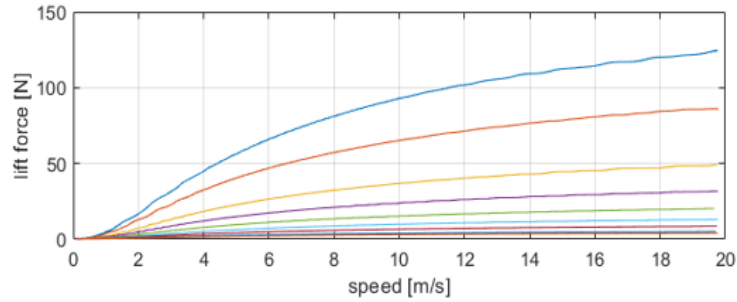
Figure 5.7: Lift and drag forces time response

5.2.4 Lift to drag ratio

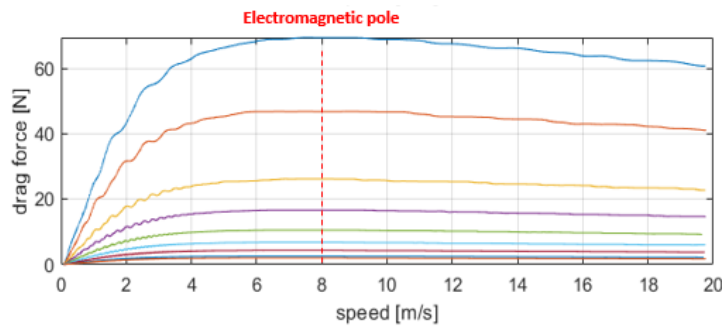
The *lift to drag ratio* is an important parameter that indicates the efficiency of the system and it can be used to verify how accurate is the behaviour of the Halbach array. As we can see from figure 5.10 the lift to drag ratio increases with the speed but it has not a constant behaviour for all the airgaps: for higher values of the latter we get a higher ratio; this means that the system is more efficient.

5.2.5 Scaled results

As is understandable, for physical reasons, the entire test bench was designed to replicate and study the behaviour of a real system that will be mounted on an *Hyperloop* train in a smaller scale. After obtaining the lift and drag



(a) Lift forces speed behaviour



(b) Drag Forces speed behaviour

Figure 5.8: Lift and drag forces speeds response

curves for the scaled Halbach array, via 3D FEM simulations using COMSOL Multiphysics[®], it was possible to derive a *scale factor* that correlates the data obtained above with that which could be obtained with a full-size system: the value of the *scale factor* is equal to 4 and consequently, the scaled F_l and F_d are proportional to the *scale factor*² while the velocity is proportional to the *scale factor*. Figure 5.11 shows the scaled lift and drag curves.

5.2.6 COMSOL simulation and experimental results comparison

The behaviour of lift and drag forces are reported along with the related numerical results obtained via 3D FEM in COMSOL Multiphysics[®]. Simulation results have been obtained considering to add an offset of 0.75 mm to each nominal air gaps: this offset takes into account all the non idealities discussed in section 4.4. Figure 5.12a shows the results for the scaled pad for 4 different airgaps: as we can see, the curve overlap quite well.

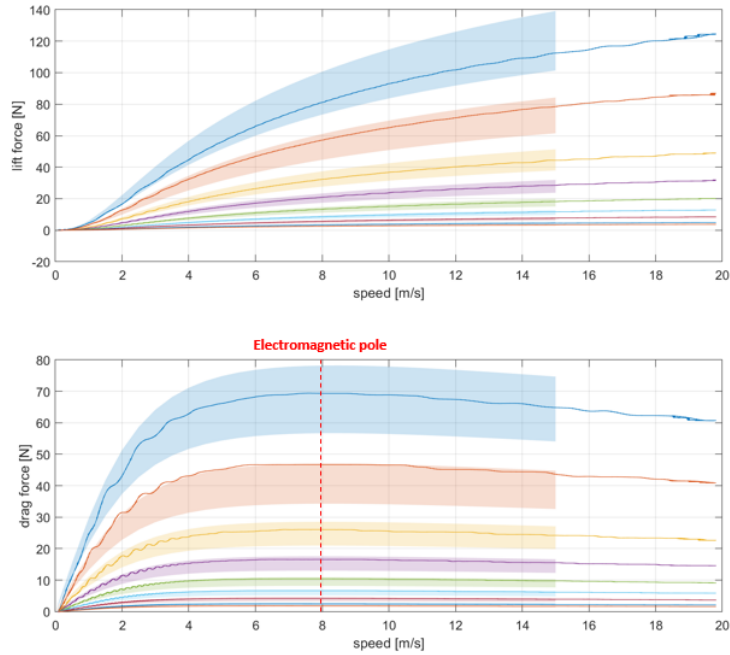


Figure 5.9: Uncertainty zone

5.2.7 Temperatures

During the experiment, the temperatures of the copper track and the pad before and after the test were monitored for each air gaps using a Fluke infrared thermometer (datasheet on Ref [38]). Table 5.1 shows the results: as expected, the largest temperature difference on the copper rim between the start and end of the test was recorded at the smallest gap ($\Delta T = 4^\circ$). Figure 5.13 shows an example of image taken by the infrared thermometer. However, it is important to emphasise that the obtained values are only indicative as they were measured on reflective materials using an infrared camera and, therefore, subject to errors.

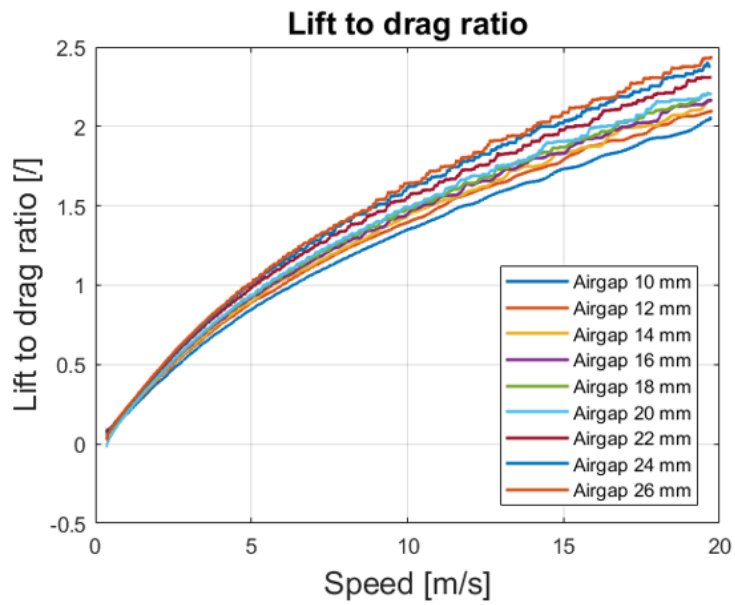


Figure 5.10: Lift to drag ratio

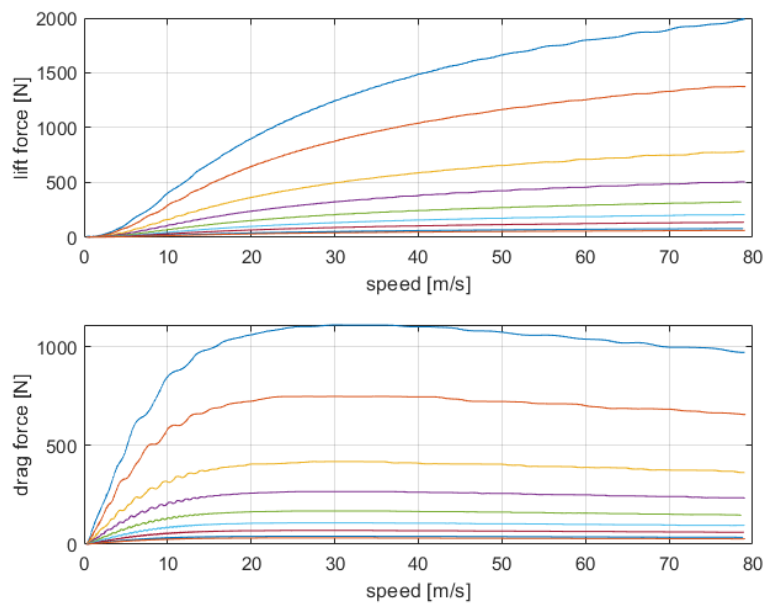
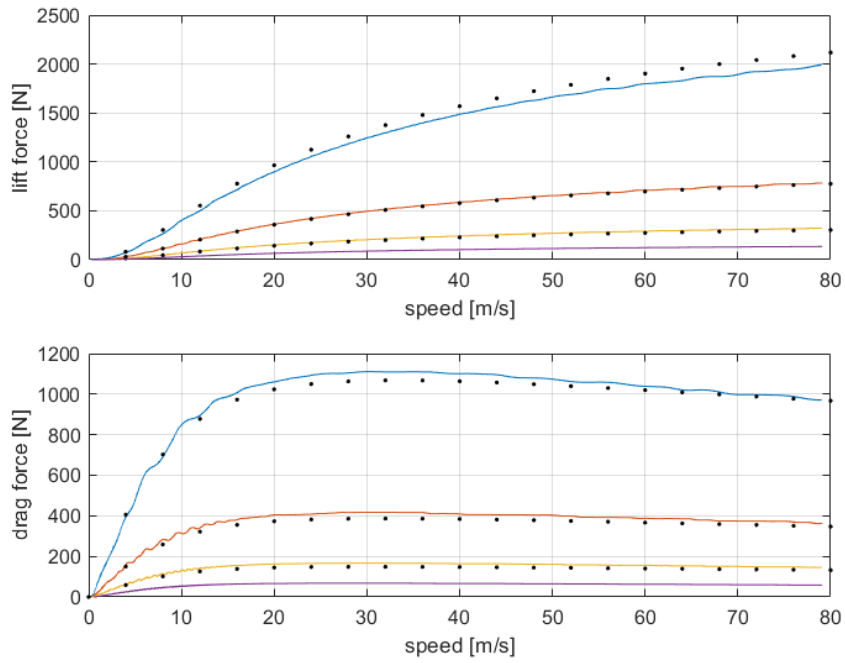
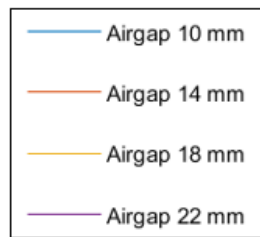


Figure 5.11: Scaled lift and drag curves



(a) Scaled lift and drag curves vs COMSOL simulations



(b) Air gaps legend

Figure 5.12: Scaled lift and drag curves behaviour

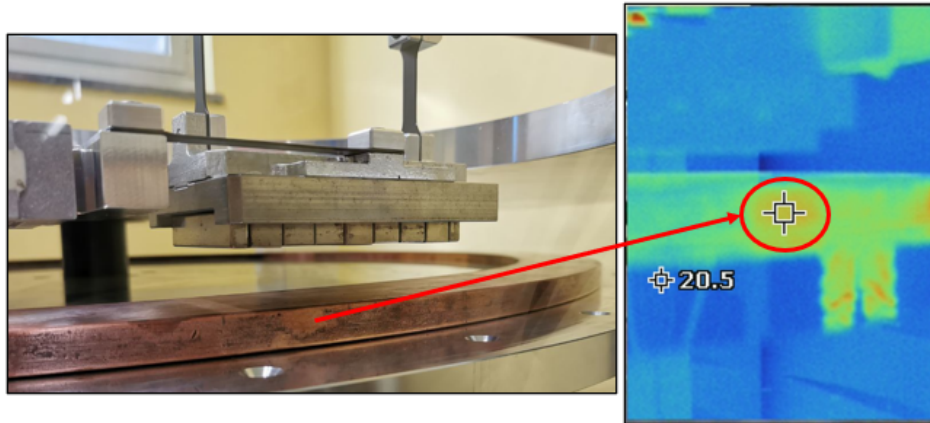


Figure 5.13: Example of Fluke temperature image

Gap [mm]	Copper track [°]		Pad [°]	
	Start	End	Start	End
10	23	27	20.9	21.3
12	21.6	23	20.7	20.9
14	21.8	21.6	21.4	20.7
16	22.1	21.8	21.2	21.4
18	22	22.1	21.5	21.2
20	21.7	22	22.2	21.5
22	21.8	21.7	21.6	22.2
24	21.4	21.8	21.9	21.6
26	20.6	21.4	20.8	21.9

Table 5.1: Copper track and pad temperature during quasi-static experiment

Chapter 6

Dynamic analysis

6.1 Dynamic measurement system

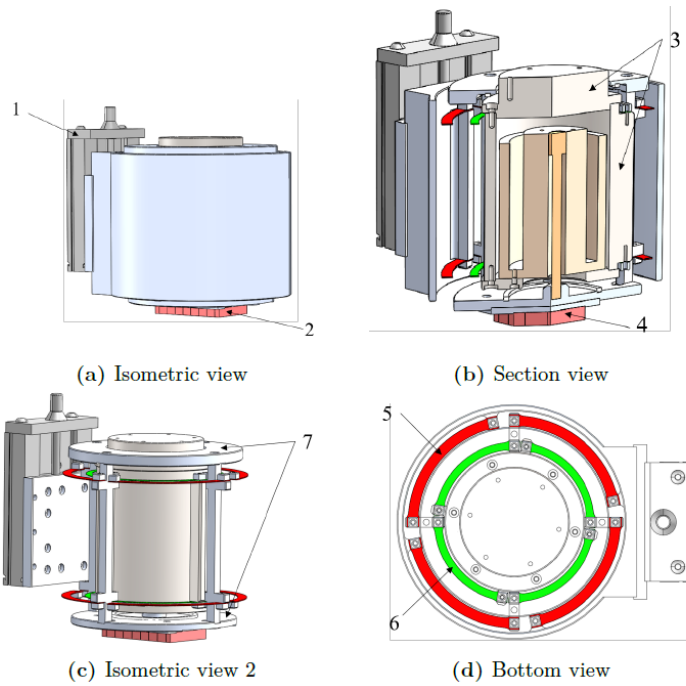
Figure 6.1a and figure 6.1b show the dynamic measurement system used to evaluate the dynamic behaviour of the levitation system:

- *micrometric linear stage* (1), as in the quasi-static experiment, is used to impose the initial airgap z_p between the copper rim and the PM array;
- *Halbach array* (2);
- *sprung* and *unsprung* masses (3 and 7 respectively);
- *secondary suspension* (4) that connects sprung and unsprung mass: in this experiment it is used a *voice coil* that can be tuned to introduce damping in the system (in section 6.4 can be found the description and the motivation of the use of a voice coil as a damper);
- *sprung-unsprung mass spring* with stiffness k_s (6) which also connects the sprung and unsprung masses: in this experiment they are two-layers of curved leaf spring to prevent relative rotation and longitudinal displacement between the capsule and the bogie;
- *stator-unsprung mass spring* with stiffness k_{us} (5), made as the previous spring, that connects the unsprung mass to the microlinear stage used as a stator.

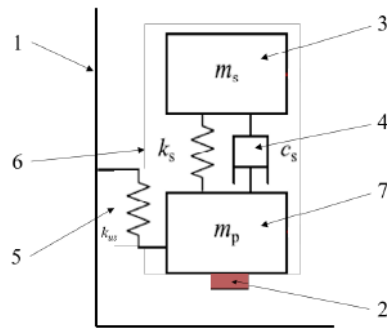
Figure 6.1b represents the classic quarter-car model whose vertical dynamics is described by equations 6.1 and 6.2.

$$\ddot{z}_p = \frac{F_{lift}}{m_p} + \frac{c_s}{m_p}(\dot{z}_s - \dot{z}_p) + \frac{k_s}{m_p}z_s - \frac{k_s + k_{us}}{m_p}z_p - g \quad (6.1)$$

$$\ddot{z}_s = -\frac{c_s}{m_s}(\dot{z}_s - \dot{z}_p) - \frac{k_s}{m_s}(z_s - z_p) - g \quad (6.2)$$



(a) Dynamic measurement system: 3D representation



(b) Dynamic measurement system: 2D representation

Figure 6.1: Dynamic measurement system

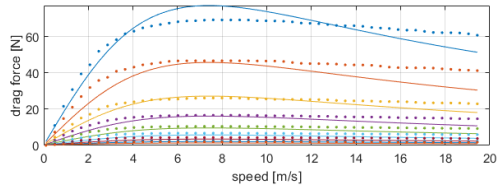
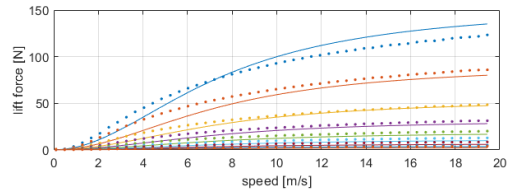
The lift force is described through the equivalent linear model while z_p and z_s are respectively the *unsprung* and *sprung* displacements. These relations can be arranged in a state-space representation as shown in Appendix A.

6.2 Fitting analysis

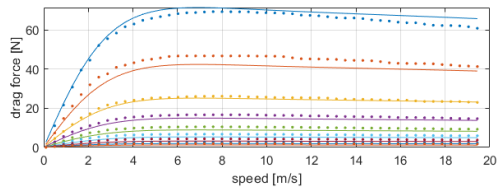
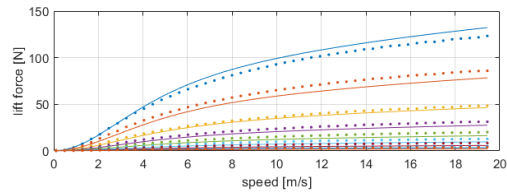
Following the multiple branches approach described in section 1.3.1 and using the lift and drag data obtained from the quasi-static experiment corrected by the interference matrix described in section 2.3.2, the fitting analysis was performed for different number of branches N_b by minimizing the l^2 -norm of the force error using MATLAB[®].

Figure 6.2 compares the experimental data (continuous lines) and the lumped-parameter model data (dots): with a single branch, the lumped-parameter model cannot reproduce the behaviour of experimental levitation system, while with a number of branches equal to 2 or 3 better results and match can be obtained.

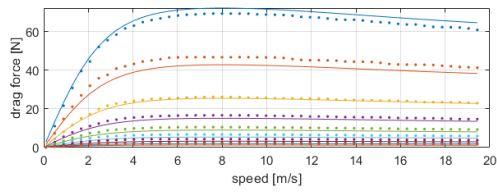
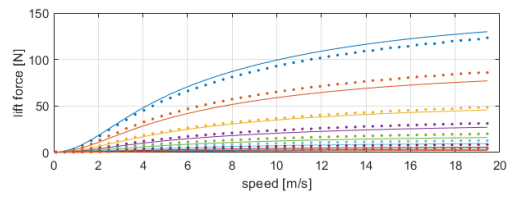
The fit error can be quantify and plot with respect to the number of branches: as expected, the fit error with a single branch is very high while it decreases with a number of branches equal to 2 and 3 (figure 6.3).



(a) $N_b = 1$



(b) $N_b = 2$



(c) $N_b = 3$

Figure 6.2: Experimental data vs lumped-parameter model

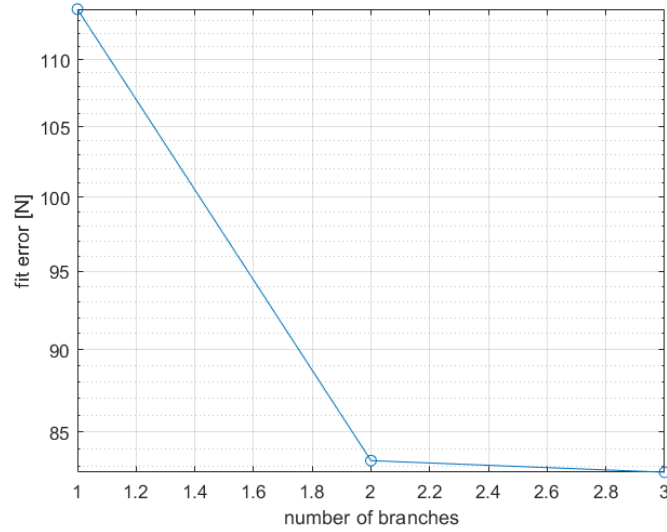


Figure 6.3: Fit error vs number of branches

Feature	Unit	$N_b = 1$	$N_b = 2$	$N_b = 3$
Fit error	N	113,92	83.34	82.67
Branch resistance	Ω	$R_1 = 59.8232$	$R_1 = 54.6679$ $R_2 = 389.3719$	$R_1 = 60.8940$ $R_2 = 217.1044$ $R_3 = 1.498e^3$
Branch inductance	H	$L_1 = 0.0617$	$L_1 = 0.0879$ $L_2 = 0.1115$	$L_1 = 0.1155$ $L_2 = 0.1349$ $L_3 = 1.0992e^{-6}$

Table 6.1: Fit error, resistance and inductance with the different number of branches

The above results can be summarized in table 6.1 with also the respectively value of resistances R and inductances L of each branch. The fit error difference between two and three branches is negligible, so $N_b = 2$ is a suitable choice.

6.3 Root locus

Considering a number of branches equal to 2 and the respectively value of resistances and inductances, different root loci at increasing v and different values of c_s are produced to tune the suspension damping and to find the optimal damping: the optimal damping is the value of damping that maximizes the horizontal distance between the poles and the imaginary axis. Figure 6.4a shows the root locus without damping: in the zoom (figure 6.4b)

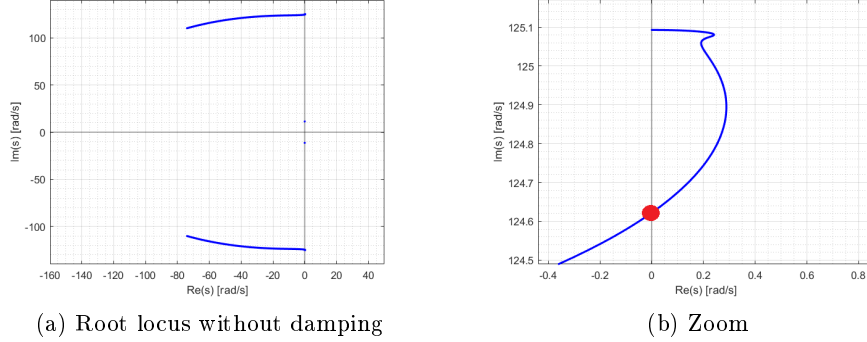


Figure 6.4: Root locus without damping

is highlighted the velocity beyond which the instability is reached: that is an angular velocity equal to 141 rpm which corresponds a linear velocity equal to 6.92 m/s.

Figure 6.5 shows a color map with different root loci: the addition of damping pushes all the mechanical poles to the left side of the complex plane (figure 6.6 shows the root locus obtained with optimal damping): with these data the optimal suspension damping c_{opt} is equal to 367.3 Ns/m (figure 6.7) and the damping ratio ζ can also be calculated as:

$$\zeta = \cos(\arctan(\frac{Im(s)}{Re(s)})) \quad (6.3)$$

6.4 Voice coil

6.4.1 General overview

The voice coil as damper was chosen for its high precision and flexibility in control: in fact, the behaviour of classic viscous dampers depends on the characteristics of the material of which they are made and the environment in which they have to work: for example, an increase in temperature due to heat dissipation could change their action, causing damage to the system. Voice coil is an electromagnetic linear actuator composed by a coil surrounded by magnets (figure 6.8): this two elements can move relative to each other so that the solenoid is subject to Lorentz force.

The voice coil can be modelled with a mechanical and electrical domain that depends on each other with the following relations:

$$F(t) = K_m i(t) \quad (6.4)$$

$$e(t) = L \frac{di(t)}{dt} + Ri(t) + K_m v(t) \quad (6.5)$$

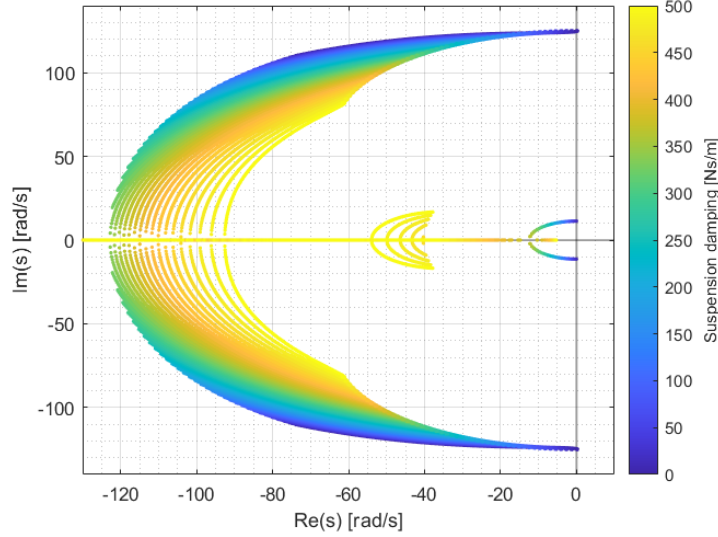


Figure 6.5: Root locus as a function of the suspension damping

K_m is the force constant that takes into account the magnetic field \vec{B} and the coil geometry through its average radius r and number of windings N : the formula, in fact, is: $K_m = 2\pi BrN$.

Equation 6.5 is the Kirchoff voltage law that relates the relative velocity $v(t)$ between the magnets and the coil with the voltage $e(t)$ and the current $i(t)$ that flows through the solenoid, corrected by the same K_m and parasitic inductance L and resistance R . The term $K_m v(t)$ represents the back EMF of the circuit (e_{VC} in figure 6.8).

The voice coil chosen for the experimental test bench is VM108-2P30-1000 by GeeplusTM (datasheet on Ref. [39]) (figure 6.9) whose main characteristics are reported in table 6.2.

Feature	Expression	Value	Unit
Resistance	R	1.3	Ω
Inductance	L	N.A.	H
Force constant	K_m	25	$\frac{N}{A}$
Maximum output current	I_{max}	7.7	A
Peak force	F_{max}	230	N
Total mass	$MTOT$	8	kg
Coil mass	m_c	0.75	kg

Table 6.2: Voice coil GeeplusTM parameters

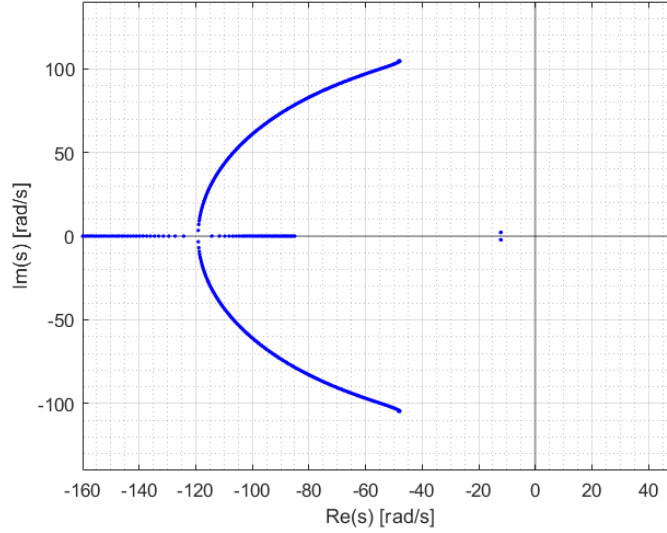


Figure 6.6: Root locus with optimal damping

6.4.2 Voice coil characterization

Intrinsic damping characterization

Since the voice coil GeeplusTM moving part is made by solid aluminum, when it moves, it generates *eddy currents damping effect*: this means that the voice coil itself has an *intrinsic* damping c that must be characterized in order to performed an accurate control of the system.

In order to evaluate it, an open circuit test was performed; first of all, the back electromagnetic force behaviour was measured through an oscilloscope during the free fall phase of the mover (figure 6.10a): focusing only on the phase where descent velocity could be considered constant, the back EMF was filtered (the red curve in figure 6.10b) and then changed sign to facilitate analysis (figure 6.10c). Subsequently, since it is an open circuit test, there is no current flow in the voice coil: by eliminating the current term in the equation 6.5, the descent velocity can be derived as $v = \frac{BackEMF}{K_m}$ and its trend can be plot (figure 6.10d).

Considering the second Newton's law during the fall phase of the voice coil, equation 6.6 can be written, from which the damping value and its trend can be extrapolated (equation 6.7 and figure 6.10e). So, the intrinsic damping value of the voice coil c is equal to 207 Ns/m.

$$m\dot{v} = mg - cv \quad (6.6)$$

$$c = \frac{mg - m\dot{v}}{v} \quad (6.7)$$

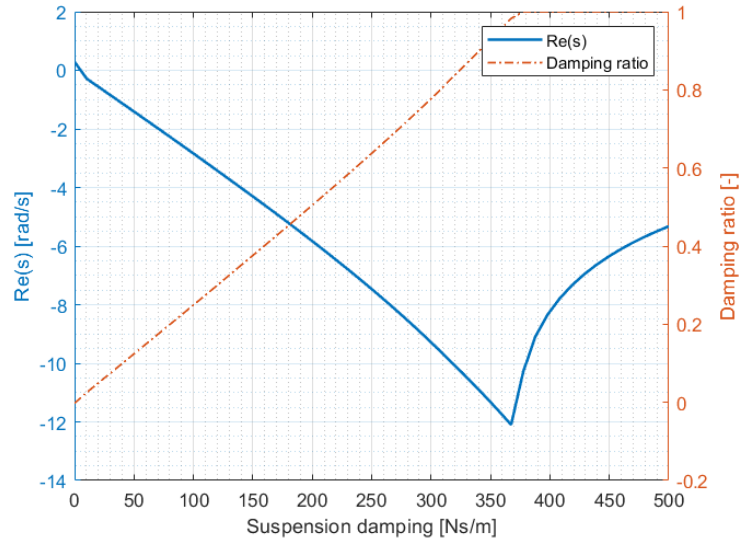


Figure 6.7: Optimal suspension damping and damping ratio

R and L characterization

Even if the datasheet provides a value of resistance, it was noticed that the resistance and inductance, when the voice coil moves, change their values depending on the relative position between the coil and the magnets. Although it is a very difficult task, an attempt has been made to characterise these values more specifically.

To estimate R and L, the voice coil was energized with constant voltage steps and held in its fully retracted position (figure 6.11). The test was performed with 6 different voltage amplitude steps. Performing the fitting using the RL equation on the experimental data and MATLAB[®], R and L were estimated. The equation used during the fitting is the following:

$$I(t) = I \cdot (1 - e^{-\frac{R}{L}t}) \quad (6.8)$$

The results are summarized in table 6.3: it is quite evident how the values of R and L vary. Moreover, as the graph in the figure 6.12 shows, there is a small discrepancy between the curve obtained by the fitting and the one of the measured data due to non linear magnetic phenomena.

If control strategies requires a single value of R and L, they could be calculated with an arithmetic mean of the reported values, although it would introduce an approximation error; therefore the mean value of R and L will be respectively 1,43 Ω and 11,1 mH.

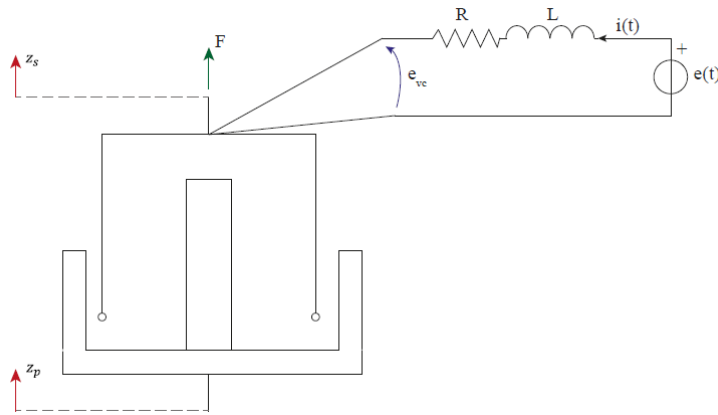


Figure 6.8: Voice coil schematic representation



Figure 6.9: Voice coil Geeplus™

Voltage	Current [A]	R/L	Resistance [Ω]	Inductance [mH]
0.59 V	0.409	190.1	1.46	7.7
1.25	0.904	147.6	1.38	9.3
2.03	1.403	120.9	1.45	11.9
2.86	1.945	120.4	1.47	12.2
3.67	2.537	120.5	1.45	11.9
4.52	3.187	106.2	1.42	13.4

Table 6.3: Voice coil fitting parameters

6.5 Control strategies

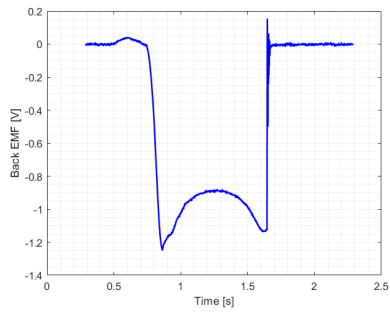
In the following sections, two possible control strategies are illustrated. They are based on two different estimators of the velocity of the voice coil, that is one of the key to control and stabilise the system.

6.5.1 RL estimator circuit

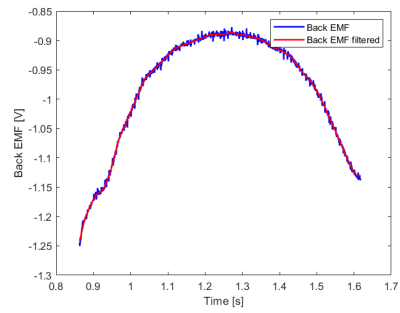
The first control strategy uses the RL circuit of the voice coil (figure 6.8) to estimate the velocity. In section 6.4.1 was already analyse the RL circuit through equation 6.5 from which it is possible to extrapolated the velocity as following:

$$v(t) = (e(t) - L \frac{di(t)}{dt} - Ri(t)) \frac{1}{K_m} \quad (6.9)$$

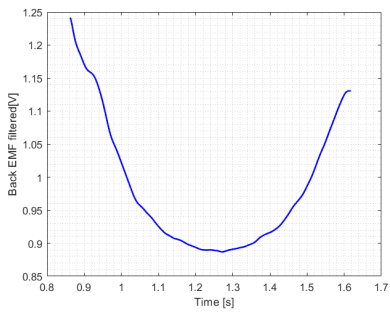
In MATLAB[®] and in SIMULINK[®] it is possible to build two different blocks that represent the voice coil circuit and the RL estimator circuit. From the first one (figure 6.13) it is possible to extrapolate the value of current and force of the voice coil: the voice coil current is sent to the RL estimator (figure 6.14) whose output is the estimated voice coil velocity; the force is,



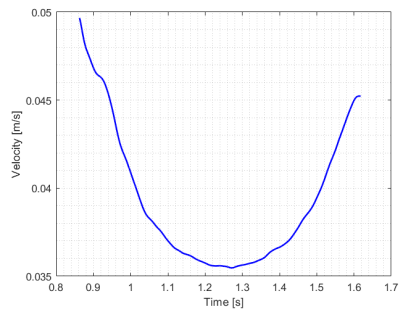
(a) Back electromagnetic force trend



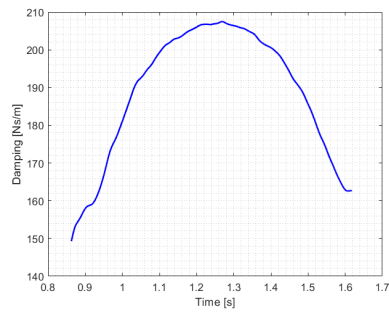
(b) Back electromagnetic zoom



(c) Back electromagnetic force after sign change



(d) Voice coil velocity



(e) Voice coil damping

Figure 6.10: Voice coil intrinsic damping characterization

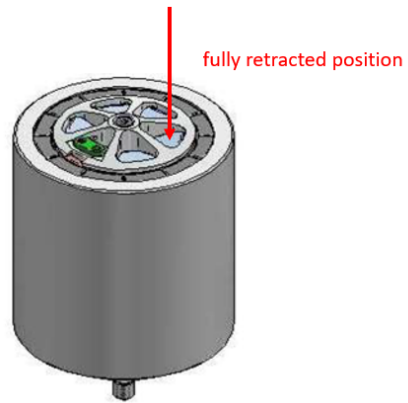


Figure 6.11: Voice coil fully retracted position

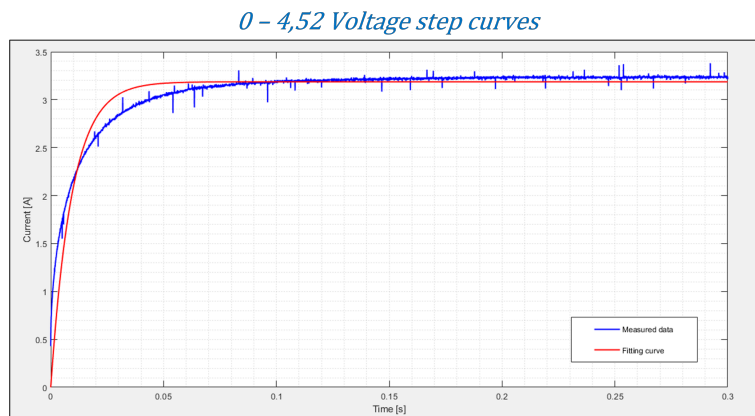


Figure 6.12: 0 - 4.52 Voltage step curves example

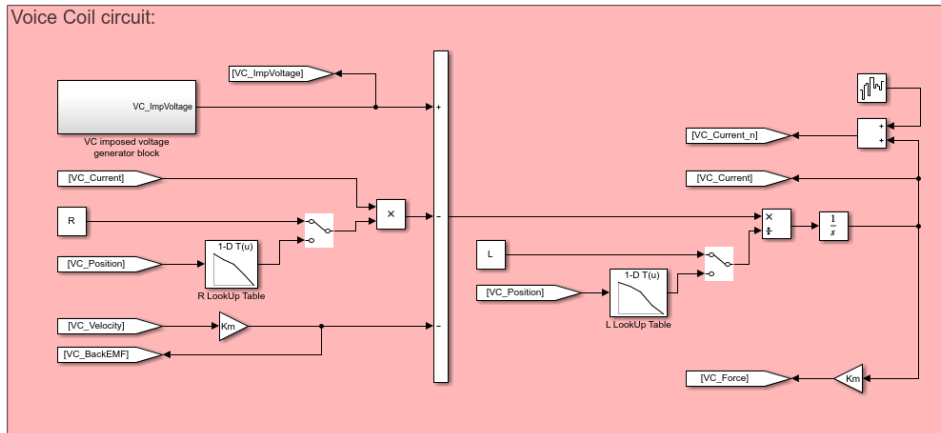


Figure 6.13: SIMULINK[®]Voice coil circuit

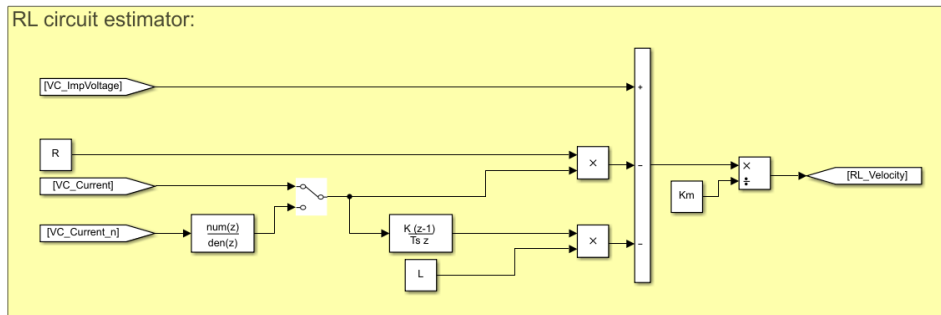


Figure 6.14: SIMULINK[®]RL circuit estimator

instead, sent to a third block that represents a MultibodyTM of the voice coil that simulates the real behaviour of the damper and from which the real voice coil velocity is extrapolated (figure 6.15).

If we analyse figure 6.13 and figure 6.14 it is possible to see that in the voice coil circuit there are two lookUp tables: they simulate the variation of the resistance and of the inductance as a function of the position of the mover of the voice coil with respect to the stator. The RL circuit, instead, requires a single value of resistance and inductance: they are set as described in section 6.4.2. In addition, in the MultibodyTM, it is possible to set a mechanical disturbance on the voice coil through a *Chirp signal*.

In order to see the accuracy of the RL estimator, two simulations are performed.

In the first one, a voice coil disturbance is set at almost 10 second but it is not considered noise on the current that, for example, can affect a physical measurement. In figure 6.16 are represented the voice coil real velocity (derived from the MultibodyTM, blue line) and the RL estimated one (orange line): even if the disturbance is followed by the estimator and the magni-

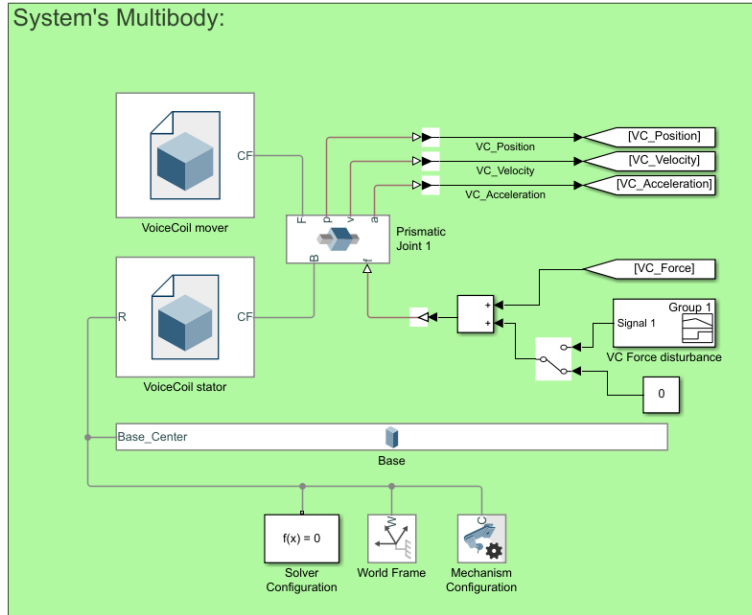


Figure 6.15: MultibodyTMvoice coil

tude is estimated quite well, there is discrepancy in the phase that is well represented in the Bode in figure 6.17: the phase difference increases with the frequency reaching 2° of shift.

In the second simulation, in addition to the disturbance, is also taken into account the current noise. Figure 6.18 and figure 6.19 show the results: with respect to the previous case, the magnitude estimation gets worse and also the phase shift is increased reaching peaks of almost -11° and 8°.

6.5.2 Kalman Filter estimator

Since good results were not achieved with the RL estimator, a new one based on the Kalman Filter was implemented. The Kalman filter algorithm combines the information from the predictions and measurements to provide the best possible estimate of the new states [40]: based on Gaussian probability density functions, it corrects the states using two covariance matrices, Q and R; matrix Q takes into account the noise on the states, while matrix R takes into account the noise on the measurements, given, for example, by sensors. For our system, we have to write the mechanical (equation 6.10) and the electrical domain equations (equation 6.5).

$$m\ddot{x} = -c\dot{x} - mg + K_m i \quad (6.10)$$

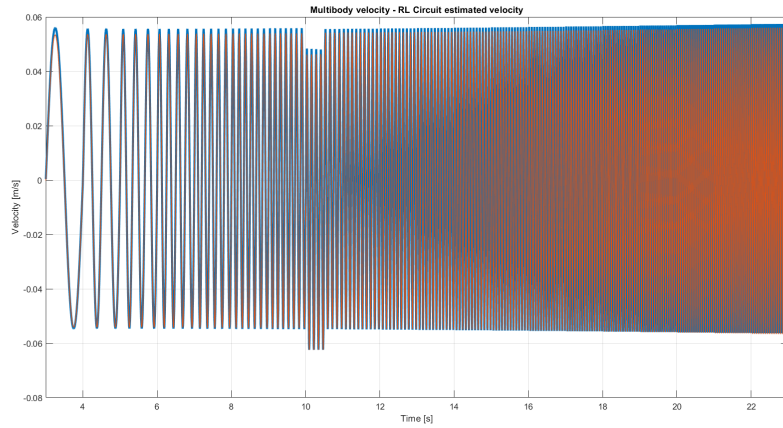


Figure 6.16: MultibodyTM velocity and RL estimated velocity without noise

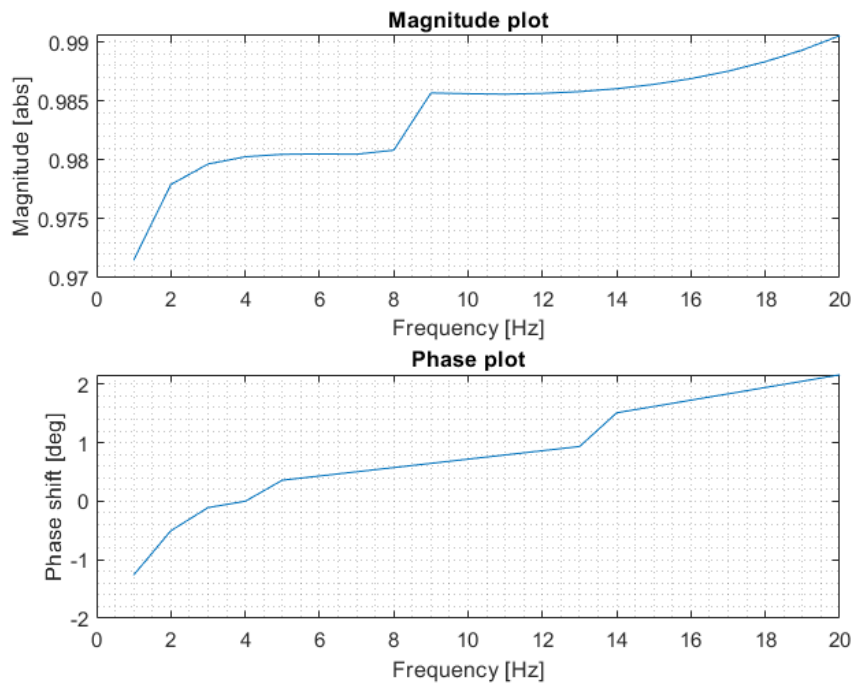


Figure 6.17: Magnitude and phase Bode of RL estimator without noise

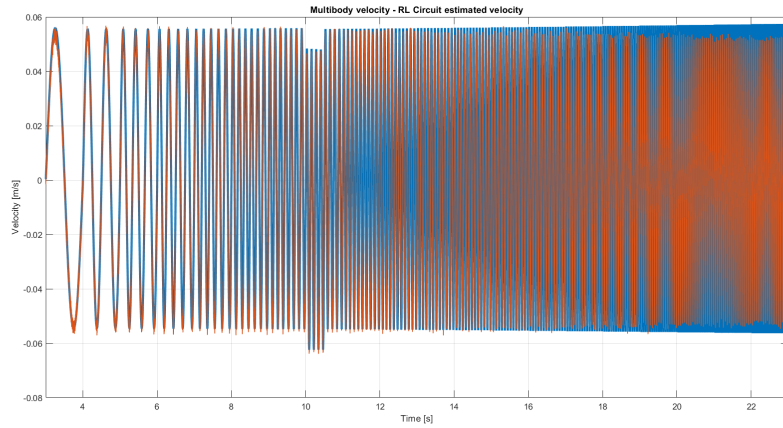


Figure 6.18: MultibodyTM velocity and RL estimated velocity with noise

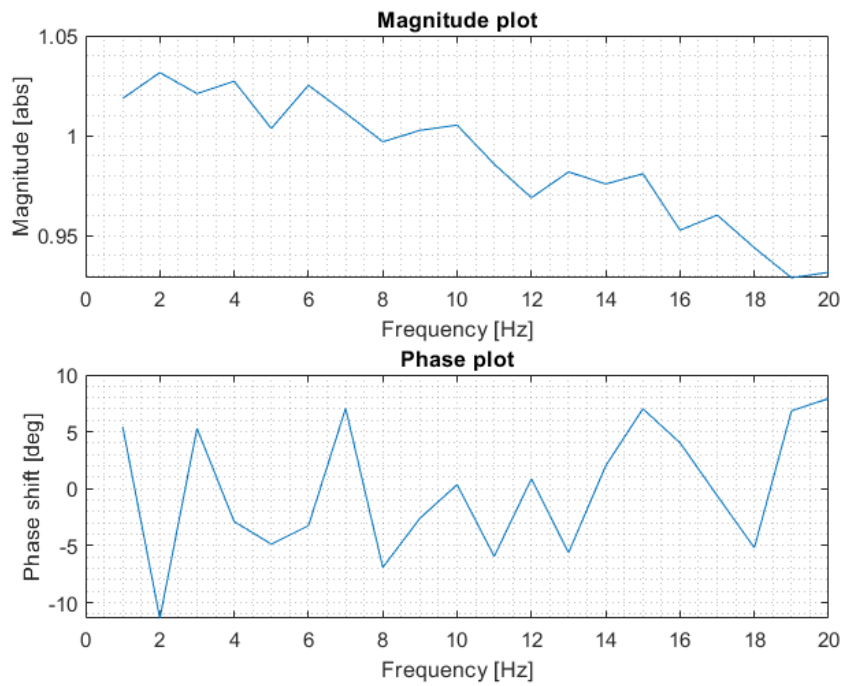


Figure 6.19: Magnitude and phase Bode of RL estimated velocity with noise

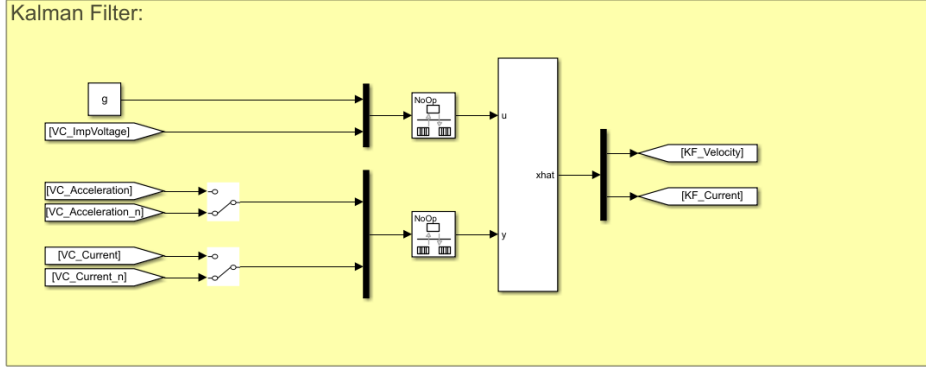


Figure 6.20: SIMULINK[®]Kalman Filter

Rewritten in state space representation, they become:

$$\begin{bmatrix} \ddot{x} \\ \frac{di}{dt} \end{bmatrix} = \begin{bmatrix} -\frac{c}{m} & \frac{K_m}{m} \\ -\frac{K_m}{L} & -\frac{R}{L} \end{bmatrix} \begin{bmatrix} \dot{x} \\ i \end{bmatrix} + \begin{bmatrix} -1 & 0 \\ 0 & \frac{1}{L} \end{bmatrix} \begin{bmatrix} g \\ e(t) \end{bmatrix} \quad (6.11)$$

$$\dot{x}_{KF} = Ax + Bu_{KF} \quad (6.12)$$

$$\begin{bmatrix} \dot{x} \\ i \end{bmatrix} = \begin{bmatrix} -\frac{c}{m} & \frac{K_m}{m} \\ 0 & 1 \end{bmatrix} \begin{bmatrix} \dot{x} \\ i \end{bmatrix} + \begin{bmatrix} -1 & 0 \\ 0 & 0 \end{bmatrix} \begin{bmatrix} g \\ e(t) \end{bmatrix} \quad (6.13)$$

$$y_{KF} = Cx + Du_{KF} \quad (6.14)$$

Using MATLAB[®], matrices A, B, C, D are discretized and inserted in the Kalman Filter block in SIMULINK[®] with u_{KF} and y_{KF} (figure 6.20) from which the estimated voice coil velocity and current are extrapolated. This block requires also the Q and R matrices that, through a trial and error procedure, are set as follows:

$$Q = \begin{bmatrix} 0.1 & 0 \\ 0 & 0.001 \end{bmatrix} \quad (6.15)$$

$$R = \begin{bmatrix} 0.001 & 0 \\ 0 & 0.001 \end{bmatrix} \quad (6.16)$$

As before, the current and the force are obtained from the voice coil circuit and the latter is sent to the MultibodyTMcircuit. Even in this case, two simulations are performed. In the first simulation, are taken into account the RL variation and a voice coil disturbance without noise on the current and on the acceleration. The results are represented in figure 6.21 and figure 6.22: especially from the Bode diagram, there is a clear improvement in results compare to the RL estimator both for the magnitude and the phase, even if the Kalman filter is not able to follow the impulse force, since it is not a gaussian disturbance.

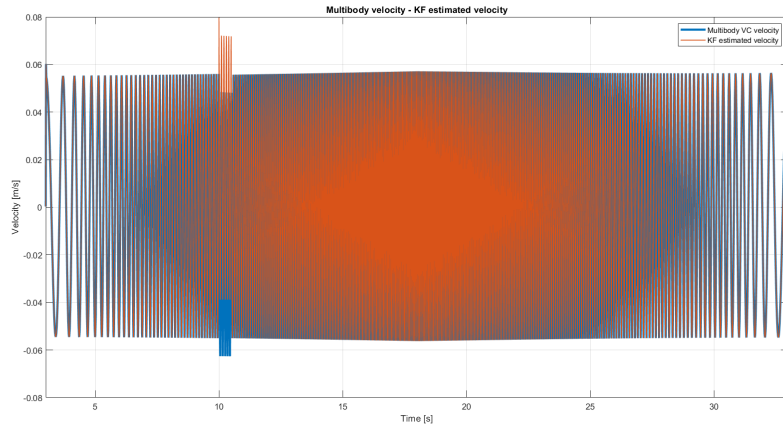


Figure 6.21: MultibodyTM velocity and KF estimated velocity without noise

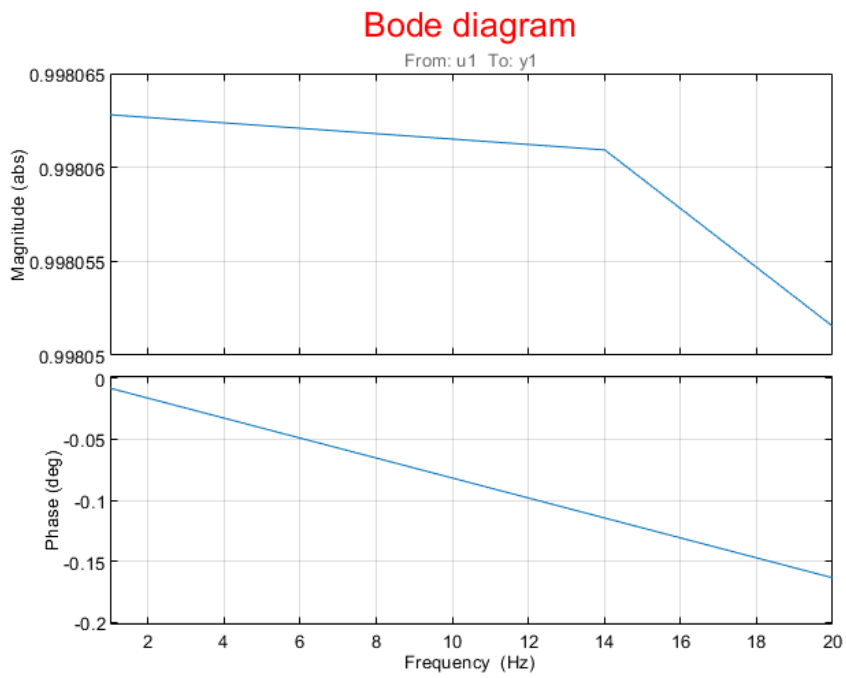


Figure 6.22: Magnitude and phase Bode of KF estimator without noise

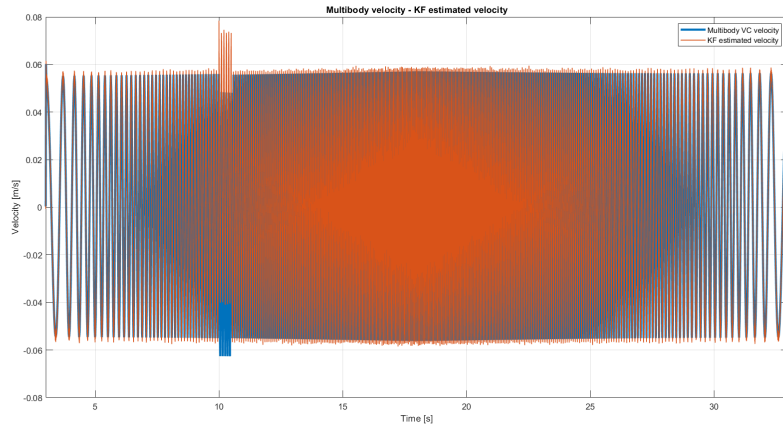


Figure 6.23: MultibodyTM velocity and KF estimated velocity with noise

In the second simulation, it is added noise to the current and acceleration measurements. Also in this case, better results can be achieved (figure 6.23 and figure 6.24).

6.5.3 Comparison between RL and KF estimator

The inaccurate RL estimation of the velocity is due to the uncertainty on the values of resistance and inductance: in fact, since the estimator needs only a value of resistance and inductance, they were put equal to the mean value calculated as in section 6.4.2. However, this leads to the introduction of an error in the estimation as the two quantities actually vary depending on the position of the mover with respect to the stator. Furthermore, the shift phase is very dangerous for the control strategy, because it means that the controller would lag behind the change in the system it is supposed to control (in this case the speed of the voice coil) leading to even more unexpected behaviour. The Kalman filter use improves the results because it is able to compensate the uncertainty of the resistance and inductance, except when an impulse force is applied.

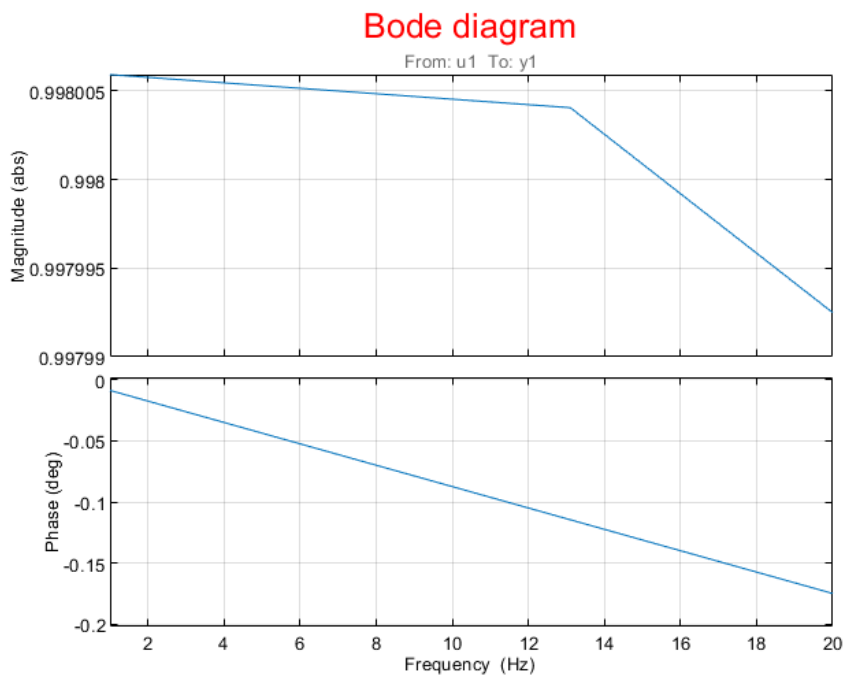


Figure 6.24: Magnitude and phase Bode of KF estimator with noise

Chapter 7

Conclusions and further studies

Two very important aspects for the feasibility of the project *Hyperloop Transportation Technologies* were illustrated in this thesis: a quasi-static analysis using a test bench was performed and a dynamic analysis.

In order to better analyse the experimental results, load cells, aluminum disk and copper rim were characterized. For the first ones, was modelled the interference between the measurements in the two directions and computed numerically the interference matrix used to correct the results.

Regarding the aluminum rotor and the copper rim, was noticed that they are not planary: the first one has a peak of 0.5 mm while the second one has more irregular surface with peaks of -0.5 to 0.3 mm.

Furthermore, the procedure to create the 90° Halbach array needed for the experiment was explained and the related sources of non idealities were illustrated such as pad inclination with respect to the copper rim, eddy currents, no negligible edge effects, air gap uncertainty due to pad vibrations, copper rim not rectified and aluminum rotor not balanced.

One of the main chapter focuses on the quasi-static experiment: it was performed at ω_{ref} equal to 400 rpm and with 9 different airgaps. The behaviour of the lift and drag forces were extrapolated. The lift force increases with the speed and its magnitude increases with smaller gaps; the drag force, instead, increases up to the electromagnetic pole which is around 163 rpm and then decreases. Furthermore, the *lift to drag ratio* was computed: it increases with the speed, but it has not a constant behaviour for all the airgaps (for higher airgaps we have found higher ratio values); in addition, using COM-SOL simulations *scaled factor* equal to 4 was derived and consequently, the scaled F_l and F_d are proportional to the *scale factor*² while the velocity is proportional to the *scale factor*.

The last chapter concentrates on the dynamic part: the fitting analysis was performed on the experiment data obtained in quasi-static conditions following the multiple branches approach. The number of branches that minimizes the error between the experimental data and the lumped-parameter model

is equal to 2. The root locus, instead, showed a velocity instability equal to 6.92 m/s without damping, while a value of optimal damping equal to 367 Ns/m.

Then, the use of a voice coil as a damper was justified and an attempt was made to characterise its most important quantities such as resistance, inductance, and intrinsic damping, which do not remain linear during its operation time. In fact, we have seen that this device has a moving part made by aluminum so, when it moves, it generates *eddy currents*: after a few steps, an intrinsic damping value was found equal to 207 Ns/m. The resistance and inductance values were, instead, extrapolated when the voice coil was energized with different voltage steps and held in its fully retracted position: a single value was calculated with an arithmetic mean.

Finally, two possible control solutions were implemented: the goal is to estimate accurately the voice coil velocity. The first one uses a RL estimator based on the RL circuit equation of the voice coil: this technique introduces a shift phase between the real and the estimated velocity that cannot be neglected because it would lead to a dangerous behaviour of the controller. The second solution, instead, uses a Kalman Filter estimator: with this technique better results can be achieved both for the magnitude (except when an impulse force is applied since it is not a gaussian disturbance) and the phase. Future studies could focus on analysing different configurations of Halbach arrays and see if they could achieve better results in terms of lift and drag curves. Furthermore, different control strategies could be implemented to reach more efficient controls.

Appendix A

2 DOF state-space representation for stability analysis

$$\mathbf{x} = \{i_{d,1} \quad i_{q,1} \quad \dots \quad i_{d,N_b} \quad i_{q,N_b} \quad z_p \quad z_p \quad \dot{z}_s \quad z_s\}^T \quad (\text{A.1})$$

$$\mathbf{A} = \begin{bmatrix} A_{el} & A_{ep} \\ A_{pe} & A_m \end{bmatrix} \quad (\text{A.2})$$

$$A_{el} = \begin{bmatrix} -\omega_{p,1} & \omega & 0 & \dots & 0 & 0 \\ -\omega & -\omega_{p,1} & 0 & \dots & 0 & 0 \\ \vdots & \vdots & \vdots & \ddots & \vdots & \vdots \\ 0 & 0 & 0 & \dots & -\omega_{p,N_b} & \omega \\ 0 & 0 & 0 & \dots & -\omega & -\omega_{p,N_b} \end{bmatrix} \quad (\text{A.3})$$

$$A_{ep} = \begin{bmatrix} \frac{\Lambda_0}{\gamma L_1} e^{-\frac{z_{p,0}}{\gamma}} & 0 & 0 & 0 \\ 0 & \omega \frac{\Lambda_0}{\gamma L_1} e^{-\frac{z_{p,0}}{\gamma}} & 0 & 0 \\ \vdots & \vdots & \vdots & \vdots \\ \frac{\Lambda_0}{\gamma L_{N_b}} e^{-\frac{z_{p,0}}{\gamma}} & 0 & 0 & 0 \\ 0 & \omega \frac{\Lambda_0}{\gamma L_{N_b}} e^{-\frac{z_{p,0}}{\gamma}} & 0 & 0 \end{bmatrix} \quad (\text{A.4})$$

$$A_{pe} = \begin{bmatrix} \frac{-2\Lambda_0}{\gamma m_p} e^{-\frac{z_{p,0}}{\gamma}} & 0 & \dots & \frac{-2\Lambda_0}{\gamma m_p} e^{-\frac{z_{p,0}}{\gamma}} & 0 \\ 0 & 0 & \dots & 0 & 0 \\ 0 & 0 & \dots & 0 & 0 \\ 0 & 0 & \dots & 0 & 0 \end{bmatrix} \quad (\text{A.5})$$

$$A_m = \begin{bmatrix} -\frac{c_s}{m_p} & -\frac{k_s+k_{us}}{m_p} & \frac{c_s}{m_p} & \frac{k_s}{m_p} \\ 1 & 0 & 0 & 0 \\ \frac{c_s}{m_s} & \frac{k_s}{m_s} & -\frac{c_s}{m_s} & -\frac{k_s}{m_s} \\ 0 & 0 & 1 & 0 \end{bmatrix} \quad (\text{A.6})$$

Bibliography

- [1] Marelli, L., Tsakalidis, A., Gkoumas, K., Haq, A., Grosso, M., and Pekar, F., 2017, “*Strategic Transport Research and Innovation Agenda (STRIA) Roadmap Factsheets*”, [HTTPS://EC.EUROPA.EU/JRC/EN/PUBLICATION/STRATEGIC-TRANSPORTRESEARCH-AND-INNOVATION-AGENDA-STRIA-ROADMAP-FACTSHEETS](https://ec.europa.eu/jrc/en/publication/strategic-transportresearch-and-innovation-agenda-stria-roadmap-factsheets) (accessed July 14, 2022).
- [2] Mitchell van Balen et al. “*EU transport research innovation status assessment report - An overview based on the Transport Research and Innovation Monitoring and Information System (TRIMIS) database*”, Aug. 2019, DOI: 10.2760/6954.
- [3] Burkhard, N., 2014, “*Why Invent the Hyperloop?*”, [HTTP://LARGE.STANFORD.EDU/COURSES/2014/PH240/BURKHARD2](http://large.stanford.edu/courses/2014/ph240/burkhard2) (accessed July 14, 2022).
- [4] 2013 SpaceX. *Hyperloop Alpha*, [HTTPS://WWW.TESLA.COM/SITES/DEFAULT/FILES/BLOG_IMAGES/HYPERLOOP-ALPHA.PDF](https://www.tesla.com/sites/default/files/blog_images/hyperloop-alpha.pdf) (accessed July 14, 2022).
- [5] Post, R. F., and Ryutov, D., 1996, “*The Inductrack Concept: A New Approach to Magnetic Levitation*”, Lawrence Livermore National Lab., CA, Technical Report UCRL-ID-124115, May.
- [6] Kusada, S., Igarashi, M., Nemoto, K., Okutomi, T., Hirano, S., Kuwano, K., Tominaga, T., Terai, M., Kuriyama, T., Tasaki, K., Tosaka, T., Marukawa, K., Hanai, S., Yamashita, T., Yanase, Y., Nakao, H., and Yamaji, M., 2007, “*The Project Overview of the HTS Magnet for Superconducting Maglev*”, IEEE Trans. Appl. Superconduct., 17(2), pp. 2111–2116.
- [7] Alexander, N. A., and Kashani, M. M., 2018, “*Exploring Bridge Dynamics for Ultra – High – Speed, Hyperloop, Trains*”, Structures, 14, pp. 69–74.

- [8] Nick, N., and Sato, Y., 2020, “*Computational Fluid Dynamics Simulation of Hyperloop Pod Predicting Laminar – Turbulent Transition*”, *Railway Eng. Sci.*, 28(1), pp. 97–111.
- [9] Choi, S. Y., Lee, C. Y., Jo, J. M., Choe, J. H., Oh, Y. J., Lee, K. S., and Lim, J. Y., 2019, “*Sub – Sonic Linear Synchronous Motors Using Superconducting Magnets for the Hyperloop*”, *Energies*, 12(24), p. 4611.
- [10] Sun, L., Taylor, J., Guo, X., Cheng, M., and Emadi, A., 2020, “*A Linear Position Measurement Scheme for Long–Distance and High–Speed Applications*”, *IEEE Trans. Industrial Electron.*, pp. 1–1.
- [11] Eric Chaidez, Shankar P. Bhattacharyya, and Adonios N. Karpetsis. “*Levitation Methods for Use in the Hyperloop High – Speed Transportation System*”, *Energies* 12.21 (2019), issn: 1996-1073, DOI: 10.3390/EN12214190, [HTTPS://WWW.MDPI.COM/1996-1073/12/21/4190](https://www.mdpi.com/1996-1073/12/21/4190) (accessed July 14, 2022).
- [12] Tonoli, A., 2007, “*Dynamic Characteristics of Eddy Current Dampers and Couplers*”, *J. Sound Vib.*, 301(3–5), pp. 576–591.
- [13] Tonoli, A., Amati, N., Impinna, F., and Detoni, J. G., 2011, “*A Solution for the Stabilization of Electrodynamic Bearings: Modeling and Experimental Validation*”, *ASME J. Vib. Acoust.*, 133(2), p. 021004.
- [14] Impinna, F., Detoni, J. G., Amati, N., and Tonoli, A., 2013, “*Passive Magnetic Levitation of Rotors on Axial Electrodynamic Bearings,*” *IEEE Trans. Magn.*, 49(1), pp. 599–608.
- [15] Detoni, J., Impinna, F., Tonoli, A., and Amati, N., 2012, “*Unified Modelling of Passive Homopolar and Heteropolar Electrodynamic Bearings*”, *J. Sound Vib.*, 331(19), pp. 4219–4232.
- [16] Filatov, A., and Maslen, E., 2001, “*Passive Magnetic Bearing for Flywheel Energy Storage Systems*”, *IEEE Trans. Magn.*, 37(6), pp. 3913–3924.
- [17] Lembke, T. A., 2005, “*Design and Analysis of a Novel Low Loss Homopolar Electrodynamic Bearing*”, Ph.D. thesis, School of Electrical Engineering, KTH, Stockholm, Sweden.
- [18] Lembke, T. A., 2014, “*Review of Electrodynamic Bearings*”, ISMB14, 14th International Symposium on Magnetic Bearings, Linz, Austria, Aug. 11–14.
- [19] Lembke, T. A., 2008, “*Electrodynamic Actuator*”, Patent application WO2010064978.

- [20] Lembke, T. A., 2012, “1 – DOF Bearing Arrangement with Passive Radial Bearings and Highly Efficient Integrated Electrodynamic Dampers, *EDD*”, ISMB13, 13th International Symposium on Magnetic Bearings, Arlington, VA, Aug. 6–9, pp. 1–7.
- [21] Van Verdeghem, J., Kluyskens, V., and Dehez, B., 2017, “Five Degrees of Freedom Linear State – Space Representation of Electrodynamic Thrust Bearings”, *J. Sound Vib.*, 405(1), pp. 48–67.
- [22] R.F. Post and D.D. Ryutov, “*The Inductrack: a simpler approach to magnetic levitation*”, *IEEE Transactions on Applied Superconductivity* 10.1 (2000), pp. 901–904, DOI: 10.1109/77.828377.
- [23] Zhaoyu Guo, Jie Li, and Danfeng Zhou, “*Study of a null – flux coil electrodynamic suspension structure for evacuated tube transportation*”, *Symmetry* 11.10 (2019), p. 1239.
- [24] Jiaheng Duan et al., “*Analysis and optimization of asymmetrical double – sided electrodynamic suspension devices*”, *IEEE Transactions on Magnetics* 55.6 (2019), pp. 1–5.
- [25] Yin Chen et al., “*A 3 – D analytic – based model of a null – flux Halbach array electrodynamic suspension device*”, *IEEE Transactions on Magnetics* 51.11 (2015), pp. 1–5.
- [26] Ruiyang Wang and Bingen Yang, “*A Transient Model of Inductrack Dynamic Systems*”, *International Design Engineering Technical Conferences and Computers and Information in Engineering Conference*, Vol. 59285. American Society of Mechanical Engineers, 2019, V008T10A062.
- [27] Ruiyang Wang and Bingen Yang, “*Transient Response of Inductrack Systems for Maglev Transport: Part II – Solution and Dynamic Analysis*”, *Journal of Vibration and Acoustics* 142.3 (2020).
- [28] Renato Galluzzi et al., “*A Multi – domain Approach to the Stabilization of Electrodynamic Levitation Systems*”, *Journal of Vibration and Acoustics* 142.6 (2020).
- [29] Salvatore Circosta et al., “*Passive Multi – Degree – of – Freedom Stabilization of Ultra – High – Speed Maglev Vehicles*”, *Journal of Vibration and Acoustics* 143.6 (2021), p. 061003.
- [30] Post, R. F., 1998, “*Inductrack Demonstration Model*”, Lawrence Livermore National Lab., CA, Technical Report, UCRL-ID-129664, Feb.
- [31] SpaceX, 2016. “*SpaceX Hyperloop Test – Track Specification*”, [HTTPS://CDN.ATRAINING.RU/DOCS/TUBESPECS.PDF](https://cdn.atraining.ru/docs/tubespecs.pdf) (accessed July 14, 2022).

- [32] *AKMServo Motor selection guide*, Kollmorgen, [HTTPS://WWW.KOLLMORGEN.COM/SITES/DEFAULT/FILES/KOLLMORGEN_AKM_SERVOMOTOR_SELECTION_GUIDE.PDF](https://www.kollmorgen.com/sites/default/files/kollmorgen_akm_servomotor_selection_guide.pdf) (accessed July 14, 2022).
- [33] *HBM - S2Specifications*, [HTTPS://WWW.HBM.COM/IT/3364/S2M-AFFIDABILI-TRASDUTTORI-DI-FORZA-AD-S-DI-ALTA-PRECISIONE/](https://www.hbm.com/it/3364/s2m-affidabili-trasduttori-di-forza-ad-s-di-alta-precisione/) (accessed July 14, 2022).
- [34] *HBM - MGCPlus assistant*, [HTTPS://WWW.HBM.COM/EN/2261/MGCPLUS-DATA-ACQUISITION-SYSTEM/?PRODUCT-TYPE-NO=MGCPLUS](https://www.hbm.com/en/2261/mgcplus-data-acquisition-system/?product-type-no=MGCPLUS) (accessed July 14, 2022).
- [35] *Vogel digital dial indicator*, [HTTPS://WWW.ILEVENINSTRUMENTS.COM/EN/INDICATORS/838-DIGITAL-DIAL-GAUGE-FUNZ-PRESET-0-13X0001.HTML](https://www.ileveninstruments.com/en/indicators/838-digital-dial-gauge-funz-preset-0-13x0001.html) (accessed July 14, 2022).
- [36] *UHU Plus Endfest 300 kg*, [HTTPS://WWW.UHU.IT/PLUS-ENDFEST-300/](https://www.uhu.it/plus-endfest-300/) (accessed July 14, 2022).
- [37] *SCADAS Mobile LMS user manual*, [HTTPS://WWW.PLM.AUTOMATION.SIEMENS.COM/FR_FR/IMAGES/SIEMENS-PLM-LMS-SCADAS-BR_TCM68-221355.PDF](https://www.plm.automation.siemens.com/fr_fr/images/siemens-plm-lms-scad-as-br_tcm68-221355.pdf) (accessed July 14, 2022).
- [38] *FLUKE*, [HTTPS://WWW.FLUKE.COM/IT-IT/PRODOTTO/TERMOCAMERA/TIS75PLUS](https://www.fluke.com/it-it/prodotto/termocamera/tis75plus) (accessed July 14, 2022).
- [39] *VM108 – 2P30 datasheet*, Geeplus, [HTTPS://WWW.GEEPLUS.COM/WP-CONTENT/UPLOADS/2019/08/VOICE_COIL_MOTOR_VM108-2P30.PDF](https://www.geeplus.com/wp-content/uploads/2019/08/Voice_Coil_Motor_VM108-2P30.pdf) (accessed July 14, 2022).
- [40] R. Faragher, “*Understanding the Basis of the Kalman Filter Via a Simple and Intuitive Derivation (Lecture Notes)*”, IEEE Signal Processing Magazine, vol. 29, no. 5, pp. 128–132, Sep. 2012, DOI: 10.1109/MSP.2012.2203621.